

# “Big Three Dragons”: a $z = 7.15$ Lyman Break Galaxy Detected in [OIII] $88\ \mu\text{m}$ , [CII] $158\ \mu\text{m}$ , and Dust Continuum with ALMA

Takuya Hashimoto<sup>1,2</sup>, Akio K. Inoue<sup>1</sup>, Ken Mawatari<sup>1,3</sup>, Yoichi Tamura<sup>4</sup>, Hiroshi Matsuo<sup>2,5</sup>, Hisanori Furusawa<sup>2</sup>, Yuichi Harikane<sup>3, 10</sup>, Takatoshi Shibuya<sup>6</sup>, Kirsten K. Knudsen<sup>7</sup>, Kotaro Kohno<sup>8,9</sup>, Yoshiaki Ono<sup>3</sup>, Erik Zackrisson<sup>11</sup>, Takashi Okamoto<sup>12</sup>, Nobunari Kashikawa<sup>2,5</sup>, Pascal A. Oesch<sup>13</sup>, Masami Ouchi<sup>3,14</sup>, Kazuaki Ota<sup>15,16</sup>, Ikkoh Shimizu<sup>17</sup>, Yoshiaki Taniguchi<sup>18</sup>, Hideki Umehata<sup>8,19</sup>, and Darach Watson<sup>20</sup>.

<sup>1</sup>Department of Environmental Science and Technology, Faculty of Design Technology, Osaka Sangyo University, 3-1-1, Nagaito, Daito, Osaka 574-8530, Japan

<sup>2</sup>National Astronomical Observatory of Japan, 2-21-1 Osawa, Mitaka, Tokyo 181-8588, Japan

<sup>3</sup>Institute for Cosmic Ray Research, The University of Tokyo, Kashiwa, Chiba 277-8582, Japan

<sup>4</sup>Division of Particle and Astrophysical Science, Graduate School of Science, Nagoya

<sup>5</sup>Department of Astronomical Science, School of Physical Sciences, The Graduate University for Advanced Studies (SOKENDAI), 2-21-1, Osawa, Mitaka, Tokyo 181-8588, Japan

<sup>6</sup>Department of Computer Science, Kitami Institute of Technology, 165 Koen-cho, Kitami, Hokkaido 090-8507, Japan

<sup>7</sup>Department of Space, Earth and Environment, Chalmers University of Technology, Onsala Space Observatory, SE-439 92 Onsala, Sweden

<sup>8</sup>Institute of Astronomy, Graduate School of Science, The University of Tokyo, 2-21-1 Osawa, Mitaka, Tokyo 181-0015, Japan

<sup>9</sup>Research Center for the Early Universe, Graduate School of Science, The University of Tokyo, 7-3-1 Hongo, Bunkyo-ku, Tokyo 113-0033, Japan

<sup>10</sup>Department of Physics, Graduate School of Science, The University of Tokyo, 7-3-1 Hongo, Bunkyo, Tokyo, 113-0033, Japan

<sup>11</sup>Department of Physics and Astronomy, Uppsala University, Box 516, SE-751 20 Uppsala, Sweden

<sup>12</sup>Department of Cosmosciences, Graduates School of Science, Hokaido University, N10 W8, Kitaku, Sapporo 060-0810, Japan

<sup>13</sup>Geneva Observatory, University of Geneva, Ch. des Maillettes, 51, 1290 Versoix, Switzerland

<sup>14</sup>Kavli Institute for the Physics and Mathematics of the Universe (WPI), Todai Institutes for Advanced Study, The University of Tokyo, 5-1-5 Kashiwanoha, Kashiwa, Chiba 277-8583, Japan

<sup>15</sup>Kavli Institute for Cosmology, University of Cambridge, Madingley Road, Cambridge, CB3 0HA, UK

<sup>16</sup>Cavendish Laboratory, University of Cambridge, 19 J.J. Thomson Avenue, Cambridge, CB3 0HE, UK

<sup>17</sup>Theoretical Astrophysics, Department of Earth & Space Science, Osaka University, 1-1 Machikaneyama, Toyonaka, Osaka 560-0043, Japan

<sup>18</sup>The Open University of Japan, 2-11 Wakaba, Mihama-ku, Chiba 261-8586, Japan

<sup>19</sup>RIKEN Cluster for Pioneering Research, 2-1 Hirosawa, Wako-shi, Saitama 351-0198, Japan

<sup>20</sup>Dark Cosmology Centre, Niels Bohr Institute, University of Copenhagen, Denmark

\*E-mail: thashimoto@est.osaka-sandai.ac.jp

Received (reception date); Accepted (acceptation date)

## Abstract

We present new ALMA observations and physical properties of a Lyman Break Galaxy at  $z = 7.15$ . Our target, B14-65666, has a bright ultra-violet (UV) absolute magnitude,  $M_{UV} \approx -22.3$ , and has been spectroscopically identified in  $\text{Ly}\alpha$  with a small rest-frame equivalent width of  $\approx 4 \text{ \AA}$ . With ALMA, we have detected spatially resolved  $[\text{OIII}]$   $88 \mu\text{m}$ ,  $[\text{CII}]$   $158 \mu\text{m}$ , and dust continuum emission at  $5.8\sigma$ ,  $10.6\sigma$ , and  $5.3\sigma$  respectively. The  $[\text{OIII}]$  and  $[\text{CII}]$  lines have consistent redshifts of  $7.1520 \pm 0.0003$ , and the  $[\text{OIII}]$  luminosity,  $(28.6 \pm 4.8) \times 10^8 L_{\odot}$ , is twice higher than the  $[\text{CII}]$  luminosity,  $(13.3 \pm 1.4) \times 10^8 L_{\odot}$ . Owing to our high spatial resolution data with beam sizes of  $\approx 0''.3 \times 0''.2$  ( $0''.3 \times 0''.3$ ) in Band 6 (Band 8),  $[\text{CII}]$  and  $[\text{OIII}]$  reveal velocity gradients of  $\approx 200 \text{ km s}^{-1}$ . Based on morphologies of  $[\text{CII}]$  and rest-frame UV emission, we argue that the velocity gradient would be due to a merger event. The merger scenario is also supported from a significant dust mass,  $(1 - 6) \times 10^7 M_{\odot}$ , which cannot be easily reproduced without considering past star-formation activity. These results imply that B14-65666 is a merger induced starburst galaxy. We also measure the  $\text{Ly}\alpha$  velocity offset with respect to the ALMA lines. The value  $\Delta v_{\text{Ly}\alpha} = 772 \pm 45 \text{ km s}^{-1}$  is the largest so far detected among the  $z > 6$  galaxy population. Based on a sample of 17 galaxies with  $\Delta v_{\text{Ly}\alpha}$  measurements from this study and the literature at  $z \approx 6 - 8$ , we find that  $\Delta v_{\text{Ly}\alpha}$  values become larger for galaxies with brighter UV magnitudes or higher  $[\text{CII}]$  luminosities. These trends are consistent with the idea that the visibility of  $\text{Ly}\alpha$  during the reionization epoch is dependent of the objects' luminosities.

**Key words:** galaxies: formation — galaxies: high-redshift — galaxies: ISM

## 1 Introduction

Understanding properties of galaxies during reionization, at redshift  $z \gtrsim 6 - 7$ , is important. While a large number of galaxy candidates are selected with a dropout technique at  $z \gtrsim 7$  (e.g., Ellis et al. 2013; Bouwens et al. 2014; Oesch et al. 2018), the spectroscopic identifications at  $z \gtrsim 7$  remain difficult (e.g., Stark et al. 2017 and references therein). This is mainly due to the fact that the most prominent hydrogen  $\text{Ly}\alpha$  line is significantly attenuated by the intergalactic medium (IGM).

With the advent of Atacama Large Millimeter/Submillimeter Array (ALMA) telescope, it has become possible to detect far-infrared (FIR) fine structure lines in star-forming galaxies at  $z > 5$  (e.g., Capak et al. 2015; Maiolino et al. 2015). A most commonly used line is  $[\text{CII}]$   $158 \mu\text{m}$ , which is one of the brightest lines in local galaxies (e.g., Malhotra et al. 1997; Braucher et al. 2008). To date, 21  $[\text{CII}]$  detections are reported at  $5 \lesssim z \lesssim 7$  (Carniani et al. 2017b and references therein) (e.g., Pentericci et al. 2016; Matthee et al. 2017; Smit et al. 2018).

However, based on a compiled sample with  $[\text{CII}]$  observations at  $z \gtrsim 5$ , Harikane et al. (2017) and Carniani et al. (2017b) have revealed that  $[\text{CII}]$  may be weak for galaxies with strong  $\text{Ly}\alpha$  emission, so-called  $\text{Ly}\alpha$  emitters (LAEs; rest-frame  $\text{Ly}\alpha$

equivalent widths  $\text{EW}_0(\text{Ly}\alpha) \gtrsim 20 - 30 \text{ \AA}$ ). Harikane et al. (2017) have interpreted the trend with photoionization models of CLOUDY implemented in spectral energy distribution (SED) models of BEAGLE (Chevallard & Charlot 2016). The authors show that low metallicity or high ionization states in LAEs lead to weak  $[\text{CII}]$ . If we assume that  $z \gtrsim 7$  galaxies in general have low metallicity or high ionization states,  $[\text{CII}]$  may not be the best line to spectroscopically confirm  $z \gtrsim 7$  galaxies. Indeed, a number of null-detections of  $[\text{CII}]$  are reported at  $z \gtrsim 7$  (e.g., Ota et al. 2014; Schaerer et al. 2015; Maiolino et al. 2015; Inoue et al. 2016).

In fact, based on *Herschel* spectroscopy for local dwarf galaxies, Cormier et al. (2015) have demonstrated that  $[\text{OIII}]$   $88 \mu\text{m}$  becomes brighter than  $[\text{CII}]$  at low metallicity (see also Malhotra et al. 2001). Based on calculations of CLOUDY, Inoue et al. (2014b) also theoretically predict that  $[\text{OIII}]$  at high- $z$  should be bright enough to be detected with ALMA.

Motivated by these backgrounds, we are conducting follow-up observations of  $[\text{OIII}]$  for  $z > 6$  galaxies with ALMA. After the first detection of  $[\text{OIII}]$  in the reionization epoch in Inoue et al. (2016) at  $z = 7.21$ , the number of  $[\text{OIII}]$  detection is rapidly increasing. There are currently six galaxies with  $[\text{OIII}]$

detections at  $z \approx 6 - 9$  (Carniani et al. 2017a; Laporte et al. 2017; Marrone et al. 2018; Hashimoto et al. 2018, Y. Tamura et al. in preparation). Remarkably, Hashimoto et al. (2018) have detected [OIII] in a  $z = 9.11$  galaxy with a high significance level of  $7.4\sigma$ . Importantly, [OIII] is detected from all the targeted galaxies, i.e., the success rate is currently 100%. These results clearly demonstrate that [OIII] is a powerful tool to confirm  $z > 6$  galaxies.

Inoue et al. (2016) have also investigated the FIR line ratio at  $z > 7$ . In a combination with the null detection of [CII], the authors have shown that their  $z = 7.21$  LAE has a line ratio of  $[\text{OIII}]/[\text{CII}] > 12$  ( $3\sigma$ ). The line ratio would give us invaluable information on properties of the interstellar medium (ISM). Given the fact that [OIII] originates only from HII regions whereas [CII] originates both from HII regions and photo-dissociated regions (PDRs), Inoue et al. (2016) have interpreted the high line ratio as the  $z = 7.21$  LAE having highly ionized HII regions but less PDRs. Such properties would lead to a high escape fraction of ionizing photons, which is a key parameter to understand reionization. Therefore, it is of interest to understand if a high line ratio is common in high- $z$  galaxies (Inoue et al. 2016).

In this study, we present new ALMA observations and physical properties of an Lyman Break Galaxy (LBG) at  $z = 7.15$ . Our target, B14-65666, is a very ultra-violet (UV) bright LBG with an absolute magnitude,  $M_{\text{UV}} \approx -22.3$  (Bowler et al. 2014). With the Faint Object Camera and Spectrograph (FOCAS) on the Subaru telescope, Furusawa et al. (2016) have spectroscopically detected  $\text{Ly}\alpha$  at the significance level of  $5.5\sigma$ . The authors find that B14-65666 has a small  $\text{EW}_0(\text{Ly}\alpha)$  of  $3.7^{+1.7}_{-1.1}$  Å. In addition, based on observations with the *Hubble Space Telescope* (HST) Wide Field Camera 3 (WFC3) F140W band image, Bowler et al. (2017) have revealed that B14-65666 is comprised of two components in the rest-frame UV with a projected separation of  $\approx 2 - 4$  kpc. At high- $z$ , such a complex structure is often interpreted in terms of a merger or clumpy star formation. The authors have argued that the large star-formation rate (SFR) inferred from the UV luminosity could be naturally explained if the system is a merger-induced starburst. More recently, with ALMA Band 6 observations, Bowler et al. (2018) have detected dust continuum emission at the peak significance level of  $5.2\sigma$ , which is the third detection of dust emission in normal star-forming galaxies at  $z > 7$  (cf., Watson et al. 2015; Laporte et al. 2017 see also Knudsen et al. 2017). However, at a relatively large beam size of  $\approx 1''.1 \times 1''.4$  (FWHM) in Bowler et al. (2018), dust emission is not spatially resolved.

In ALMA Cycle 4, we have performed high spatial resolution follow-up observations of B14-65666 with beam sizes of  $\approx 0''.3 \times 0''.2$  ( $0''.3 \times 0''.3$ ) in Band 6 (Band 8). We successfully detect spatially resolved [CII], [OIII], and dust continuum emission, making B14-65666 the first object at  $z \gtrsim 6$

with a complete set of these three features<sup>1</sup>. The spatially resolved data enable us to investigate the velocity gradients of the [CII] and [OIII] lines. These emission lines also allow us to investigate the  $\text{Ly}\alpha$  velocity offset with respect to the systemic,  $\Delta v_{\text{Ly}\alpha}$ , which is an important parameter to understand reionization (e.g., Choudhury et al. 2015; Mason et al. 2017, 2018). The dust continuum emission also offers us invaluable information on the ISM properties of B14-65666. We also derive physical quantities such as the stellar age, the stellar mass ( $M_\odot$ ), and the SFR. With these quantities, we will discuss kinematical, morphological, and ISM properties of B14-65666.

This paper is organized as follows. We describe our data in §2. In §3, we measure [CII] and [OIII] quantities. Dust properties are estimated in §4, followed by results on luminosity ratios in §5. In §6, we perform spectral energy distribution (SED) fitting. In §7, we derive  $\Delta v_{\text{Ly}\alpha}$  in B14-65666, and statistically examine  $\Delta v_{\text{Ly}\alpha}$  at  $z \approx 6 - 8$ . Discussions in the context of (i) properties of B14-65666 and (ii) reionization are presented in §8, followed by our conclusions in §9. Throughout this paper, magnitudes are given in the AB system (Oke & Gunn 1983), and we assume a  $\Lambda$ CDM cosmology with  $\Omega_m = 0.272$ ,  $\Omega_b = 0.045$ ,  $\Omega_\Lambda = 0.728$  and  $H_0 = 70.4 \text{ km s}^{-1} \text{ Mpc}^{-1}$  (Komatsu et al. 2011).

## 2 Observations and Data

### 2.1 ALMA Band 6 and Band 8 Observations

In Cycle 4, we observed B14-65666 with ALMA in Band 6 and Band 8 targeting [CII]  $158 \mu\text{m}$  and [OIII]  $88 \mu\text{m}$ , respectively (ID 2016.1.00954.S, PI: A. K. Inoue). In Band 6 (Band 8), the antenna configuration was C40-6 (C40-4) and the on-source exposure times were 114 (51) minutes. Our observation strategy was the same for both bands. We used four spectral windows (SPWs) with 1.875 GHz bandwidths in the Frequency Division Mode (FDM), totaling the band width of 7.5 GHz. Two SPWs with a 7.813 MHz resolution was used to target the lines. One of the two SPWs was centered on the  $\text{Ly}\alpha$  frequency and the other was centered at a higher frequency (i.e., a shorter wavelength) with a small overlap in frequency, taking into account the possible redward velocity offset of the  $\text{Ly}\alpha$  line with respect to the systemic redshift (e.g., Steidel et al. 2010; Hashimoto et al. 2013). The remaining two SPWs with a 31.25 MHz resolution were used to observe dust continuum emission at  $\approx 163 \mu\text{m}$  and at  $\approx 90 \mu\text{m}$  in Band 6 and Band 8, respectively. Our observations are summarized in Table 1.

In both band observations, a quasar, J1058+0133, was used for bandpass calibrations. Two quasars, J1058+0133 and J0854+2006, were used for flux calibrations, and a quasar,

<sup>1</sup> “Big Three Dragons” is a hand in a *Mahjong* game with triplets or quads of all three dragons.

J0948+0022, was used for phase calibrations. The flux calibration uncertainty was estimated to be  $\lesssim 10$  (20)% in Band 6 (Band 8). The data were reduced and calibrated using the Common Astronomy Software Application (CASA) pipeline version 4.7.2 and 4.7.0 for Band 6 and Band 8 data, respectively. We produced images and cubes with the CLEAN task using the natural weighting to maximize point-source sensitivity. To create a pure dust continuum image, we collapsed all off-line channels. To create a pure line image, we subtracted continuum using the off-line channels in the line cube with the CASA task `uvcontsub`. In Table 2, we summarize the spatial resolution, the beam position angle, and the r.m.s. level for the continuum image and the line cube with a spectral bin of  $100 \text{ km s}^{-1}$ .

## 2.2 Astrometry

In the following sections, we compare spatial positions of our ALMA data with those in the archival HST F140W band image data taken by Bowler et al. (2017). Several studies have reported spatial offsets between ALMA-detected objects and their HST-counterparts either due to astrometry uncertainties or physical offsets in different wavelengths (e.g., Laporte et al. 2017; González-López et al. 2017; Carniani et al. 2017b; Dunlop et al. 2017). In order to calibrate the HST astrometry better, we first search for bright stars in the catalog `gaiadr1.gaiadr_source` released in the framework of the GAIA project<sup>2</sup> (Gaia Collaboration et al. 2016). Similar astrometry calibrations are performed in Carniani et al. (2017b). Because of the small sky area,  $\approx 2'.3 \times 2'.0$ , covered by the Bowler et al.'s archival HST data, only a single star is matched to the catalog. Thus, we instead use the catalog `gaiadr1.sdssdr9_original_valid` from the same project. The latter catalog includes a larger number of objects while its astrometry is originally taken from the SDSS project. We have used IRAF tasks `ccmap` and `ccsetwcs` for the HST astrometry<sup>3</sup>. The applied shift around B14-65666 is  $\approx 0''.25$  for the archival HST image. To check the accuracy of our astrometry, we make use of a serendipitous continuum detection ( $16\sigma$ ) in Band 6 from a galaxy at  $z = 1.93$ , COSMOS 0813412 (Schinnerer et al. 2007). Figure 1 shows that the centroids of ALMA continuum and its HST F140W counterpart are consistent with each other within  $\approx 0''.15$  uncertainties, demonstrating successful astrometry calibration<sup>4</sup>.

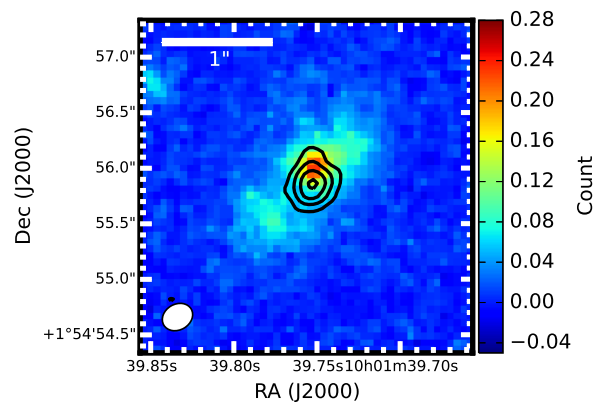


**Fig. 1.** ALMA Band 6 continuum image of a serendipitously detected object at  $z = 1.93$ , COSMOS 0813412 (Schinnerer et al. 2007), overlaid on its counterpart in the HST F140W image with re-calibrated astrometry. Contours are drawn at  $(4, 8, 12, 16) \times \sigma$ , where  $\sigma = 9.5 \mu\text{Jy beam}^{-1}$ . The ellipse at lower left indicates the synthesized beam size of ALMA.

## 3 [CII] 158 $\mu\text{m}$ and [OIII] 88 $\mu\text{m}$ lines

In Band 6 (Band8) data, to search for an emission line, we have created a data cube by binning three (six) native channels, resulting in a velocity resolution of  $\approx 30$  (33)  $\text{km s}^{-1}$ . At the B14-65666 position, we find a supposed [CII] ([OIII]) feature at around 233.12 (416.27) GHz. This frequency region is free from atmospheric absorption features. In Band 6 (Band8), we have then created a velocity-integrated intensity image between 232.9 and 233.4 GHz (416.0 and 416.6 GHz) corresponding to  $\approx 600$  (400)  $\text{km s}^{-1}$ .

The top left and bottom left panels of Figure 2 show [CII] and [OIII] contours overlaid on the F140W images, respectively. All of [CII], [OIII], and rest-frame UV images are elongated in the West-East direction. With our spatial resolution, [CII] and [OIII] are spatially resolved. Assuming a 2D Gaussian profile for the velocity-integrated intensity, we measure the beam-deconvolved size of [CII] to be  $(0''.89 \pm 0''.13) \times (0''.33 \pm 0''.06)$ , where the first and second values represent the FWHMs of the major and minor-axis, respectively. Likewise, we obtain the size of [OIII] to be  $(0''.67 \pm 0''.17) \times (0''.17 \pm 0''.14)$ .

With the velocity-integrated intensity image of [CII] ([OIII]), we obtain the peak intensity of  $0.18 \pm 0.02$  ( $0.56 \pm 0.08$ )  $\text{Jy km s}^{-1} \text{ beam}^{-1}$ . We spatially integrate the image with the CASA task `imfit` assuming a 2D Gaussian profile for the velocity-integrated intensity. For [CII] ([OIII]), we obtain the velocity-integrated line flux to be  $1.04 \pm 0.10$  ( $1.25 \pm 0.21$ )  $\text{Jy km s}^{-1}$ , corresponding to a significant level of  $10.6\sigma$  ( $5.8\sigma$ ). Because the intensity may not be well represented by a 2D Gaussian, we

<sup>2</sup> <https://gea.esac.esa.int/archive/>

<sup>3</sup> We have used 17 objects uniformly distributed in the field-of-view for the astrometry calibration.

<sup>4</sup> Due to the small field-of-view of Band 8 data, COSMOS 0813412 is not observed in Band 8. We assume that the ALMA astrometry in Band 6 and Band 8 are consistent with each other.

**Table 1.** Summary of ALMA Observations.

Date (YYYY-MM-DD)	Baseline lengths (m)	$N_{\text{ant}}$	Central frequencies of SPWs (GHz)	Integration time (min.)	PWV (mm)
(1)	(2)	(3)	(4)	(5)	(6)
<b>Band 6</b>					
2017-07-09	16 – 2647	40	218.78, 216.98, 232.66, 234.48	37.80	0.45
2017-07-09	16 – 2647	40	218.78, 216.98, 232.66, 234.48	37.80	0.44
2017-07-09	16 – 2647	40	218.78, 216.98, 232.66, 234.48	37.80	0.42
<b>Band 8</b>					
2016-11-14	15 – 919	44	405.43, 403.61, 415.47, 417.23	12.60	0.58
2016-11-15	15 – 918	40	405.43, 403.61, 415.47, 417.23	38.80	0.63

Note. (1) The observation date; (2) the ALMA's baseline length; (3) the number of antenna used in the observation; (4) the central frequencies of the four spectral windows (SPWs); (5) the on-source integration time; (6) the precipitable water vapor.

**Table 2.** Summary of ALMA data.

ALMA Band	$\sigma_{\text{cont}}$ ( $\mu\text{Jy beam}^{-1}$ )	$\sigma_{100\text{km s}^{-1}}$ ( $\mu\text{Jy beam}^{-1}$ )	Beam FWHMs (arcsec $\times$ arcsec)	Beam PA (deg.)
(1)	(2)	(3)	(4)	(5)
Band 6 (natural)	9.5	68.5	$0.29 \times 0.23$	–60
Band 6 (Briggs)	11.0	87.6	$0.23 \times 0.12$	–70
Band 8 (natural)	62.4	403.4	$0.31 \times 0.28$	44

Note. (1) The ALMA Band used. Weighting is specified in the parenthesis; (2) the  $1\sigma$  r.m.s. level of the continuum image; (3) the typical  $1\sigma$  r.m.s. level of the line cube with a  $100\text{ km s}^{-1}$  velocity bin; (4) the ALMA's beam FWHM in units of arcsec  $\times$  arcsec; (5) the ALMA's beam position angle in units of degree.

have also estimated the line fluxes by applying aperture photometry on the clean images. We find that the results are consistent with the line fluxes obtained from `imfit`.

To obtain the redshift and FWHM of the lines, we extract spectra from the [CII] and [OIII] regions with  $> 3\sigma$  detections in the velocity-integrated intensity images. The spectra of [CII] and [OIII] are shown in the top left and top right panels of Figure 3, respectively. Applying a Gaussian line profile and the rest-frame [CII] frequency of  $1900.5369\text{ GHz}$ <sup>5</sup>, we obtain the [CII] redshift of  $z = 7.1521 \pm 0.0004$  and the FWHM value of  $349 \pm 31\text{ km s}^{-1}$ . Likewise, with the [OIII] frequency of  $3393.006244\text{ GHz}$ , we obtain the [OIII] redshift of  $7.1510 \pm 0.0010$  and the FWHM value of  $448 \pm 90\text{ km s}^{-1}$ . We find that the two redshift and FWHM values are consistent with each other within  $1\sigma$  uncertainties.

To derive the line luminosity, we use the following relation

$$L_{\text{line}} = 1.04 \times 10^{-3} \times \left( \frac{S_{\text{line}} \Delta v}{\text{Jy km s}^{-1}} \right) \left( \frac{D_L}{\text{Mpc}} \right)^2 \left( \frac{\nu_{\text{obs}}}{\text{GHz}} \right) L_{\odot} \quad (1)$$

(Carilli & Walter 2013), where  $S_{\text{line}} \Delta v$  is the velocity-integrated flux,  $D_L$  is the luminosity distance, and  $\nu_{\text{obs}}$  is the observed frequency. We obtain  $(13.3 \pm 1.3) \times 10^8 L_{\odot}$  and  $(28.6 \pm 4.8) \times 10^8 L_{\odot}$  for the [CII] and [OIII] luminosity, respectively. These measurements are summarized in Table 3.

The [CII] luminosity of B14-65666 is the highest among star forming galaxies at  $z > 6$  (see Carniani et al. 2017b and references therein) and is comparable to those of [CII] emitters at

$z \sim 5$  in Capak et al. (2015). In fact, the [CII] luminosity of B14-65666 is comparable to those of two quasar host galaxies at  $z > 7$ : J1120+0641 at  $z = 7.08$  has  $(1.2 \pm 0.2) \times 10^9 L_{\odot}$  (Venemans et al. 2012) and J1342+0928 at  $z = 7.54$  has  $(1.6 \pm 0.2) \times 10^9 L_{\odot}$  (Bañados et al. 2018; Venemans et al. 2017). Likewise, the [OIII] luminosity of B14-65666 is the highest among normal star forming galaxies at  $z > 7$  (Inoue et al. 2016; Laporte et al. 2017; Carniani et al. 2017a; Hashimoto et al. 2018, Y. Tamura et al. in prep.).

### 3.1 Multiple components of [CII]

Recent ALMA studies of high- $z$  galaxies show spatially separated multiple [CII] components with projected distances of  $\approx 3 - 7\text{ kpc}$  (e.g., Matthee et al. 2017; Carniani et al. 2017b, 2018). Noting the multiple components in the HST F140W image of B14-65666 (Bowler et al. 2017), we have created a higher spatial resolution image of [CII] with Briggs weighting and a robust parameter 0.3 in the CASA CLEAN task<sup>6</sup>. The beam size of the high spatial resolution image is  $0''.23 \times 0''.12$  (FWHM; see Table 2)<sup>7</sup>. As shown in the top left panel of Figure 4, our ALMA data reveal that [CII] is comprised of at least two regions: The centroids of the two [CII] knots are well consistent with those of two rest-frame UV clumps, suggesting that [CII]

<sup>6</sup> For the description of the Briggs weighing and the robust parameter, <https://casa.nrao.edu/Release4.1.0/doc/UserMan/UserMansu262.html>

<sup>7</sup> Based on aperture photometry, we find that the higher spatial resolution image recovers  $\approx 86\%$  of the total [CII] flux, implying that the “resolved-out” effect is insignificant.

<sup>5</sup> <http://www.cv.nrao.edu/php/splat/>

is associated with star-forming regions. The North-Eastern part (“clump A”) has extended disturbed morphology and the South-Western part (“clump B”) has compact morphology.

We extract spectra from the two HST peak pixels (see the crosses in Figure 4). The middle left and bottom left panels of Figure 3 shows the [CII] spectra. Applying a Gaussian for each spectrum, we have obtained the redshift values as summarized in Table 4. Based on these two redshifts, the velocity offset between the two components is  $192 \pm 24 \text{ km s}^{-1}$ . We also create a flux-weighted velocity (i.e., Moment 1) map of [CII] with the CASA task `immoments`. In this procedure, we only include pixels above  $3\sigma$  in the velocity-integrated intensity image (c.f., Jones et al. 2017a). The bottom left panel of Figure 4 demonstrates that [CII] shows an  $\approx 200 \text{ km s}^{-1}$  velocity gradient. In addition, the clump A and clump B correspond to the positive and negative velocity peaks, respectively, within the astrometry accuracy of  $\approx 0''.15$  (see §2.2).

Likewise, the middle right and bottom right panels of Figure 3 show the [OIII] spectra extracted from the two HST peak pixels. The redshift values are summarized in Table 4. The velocity offset between the two components is  $162 \pm 40 \text{ km s}^{-1}$ , which is consistent with that for [CII]. The bottom right panel of Figure 4 also shows the velocity gradient of [OIII]. The [OIII] line also shows a velocity gradient, although it is not as clear as that of [CII] due to the low significance level of [OIII].

Based on the fact that B14-65666 has two rest-frame UV clumps, [CII] clumps, and velocity peaks whose spatial positions are consistent with each other, we infer that the system is a merger, as first claimed by Bowler et al. (2017) (see §1). A further discussion in terms of merger is presented in §8.1.

## 4 Dust

We search for dust thermal emission in the two continuum images at around 163 and 90  $\mu\text{m}$ . Hereafter, we refer to these two images as *dust163* and *dust90*, respectively.

The top right panel of Figure 2 shows contours of *dust163* overlaid on the F140W image. We have detected a signal at the F140W position. We spatially integrate the image with the CASA task `imfit` assuming a 2D Gaussian profile for the flux density. The derived flux density is  $S_{\nu,163\mu\text{m}} = 130 \pm 25 \mu\text{Jy}$  ( $S/N = 5.3$ )<sup>8</sup>. Our flux density is well consistent with the flux density at 158  $\mu\text{m}$  presented by Bowler et al. (2018),  $168 \pm 56 \mu\text{Jy}$ , taken at a lower angular resolution. However, we do not find any significant spatial offset between the dust continuum and the F140W position as claimed by them. In fact, we find that there exist a spatial offset between the centroid of our Band 6 continuum image and that of Bowler et al.’s (in private communication with R.A.A. Bowler). Although deeper dust contin-

**Table 3.** Summary of observational results of B14-65666.

Parameters	Values
R.A.	10:01:40.69
Dec.	+01:54:52.5
$M_{1500}$ [AB mag.]	-22.3
$z_{[\text{OIII}]}$	$7.1510 \pm 0.0010$
$z_{[\text{CII}]}$	$7.1521 \pm 0.0004$
$z_{\text{sys.}}^a$	$7.1520 \pm 0.0003$
$z_{\text{Ly}\alpha}^b$	$7.1730 \pm 0.0012$
$\Delta v_{\text{Ly}\alpha}$ [km s <sup>-1</sup> ]	$772 \pm 45$
FWHM([OIII]) [km s <sup>-1</sup> ]	$448 \pm 90$
FWHM([CII]) [km s <sup>-1</sup> ]	$349 \pm 31$
$S_{\nu,90}$ [ $\mu\text{Jy}$ ]	$< 370$ ( $3\sigma$ )
$S_{\nu,163}$ [ $\mu\text{Jy}$ ]	$130 \pm 25$ ( $S/N = 5.3$ )
[OIII] integrated flux [Jy km s <sup>-1</sup> ]	$1.25 \pm 0.21$ ( $S/N = 5.8$ )
[CII] integrated flux [Jy km s <sup>-1</sup> ]	$1.04 \pm 0.10$ ( $S/N = 10.6$ )
[OIII] luminosity [ $10^8 L_{\odot}$ ]	$28.6 \pm 4.8$
[CII] luminosity [ $10^8 L_{\odot}$ ]	$13.3 \pm 1.3$
Ly $\alpha$ luminosity [ $10^8 L_{\odot}$ ]	$6.8 \pm 1.3$ ( $S/N = 5.5$ )
Dust deconvolved size <sup>c</sup>	$(0''.72 \pm 0''.20) \times (0''.15 \pm 0''.01)$
[OIII] deconvolved size <sup>c</sup>	$(0''.67 \pm 0''.17) \times (0''.17 \pm 0''.01)$
[CII] deconvolved size <sup>c</sup>	$(0''.89 \pm 0''.13) \times (0''.33 \pm 0''.06)$

Note. <sup>a</sup> The systemic redshift,  $z_{\text{sys.}}$ , is calculated as the  $S/N$ -weighted mean redshift of  $z_{[\text{OIII}]}$  and  $z_{[\text{CII}]}$ .

<sup>b</sup> The value is different from the original value in Furusawa et al. (2016),  $z_{\text{Ly}\alpha} = 7.168$ , to take into account air refraction and the motion of the observatory (see §7).

<sup>c</sup> The values represent major and semi-axis FWHM values of a 2D Gaussian profile.

uum data are required, it is possible that there exist extended dust emission which cannot be traced by our high-angular resolution data.

Thanks to our higher spatial resolution data, we have for the first time resolved the dust continuum emission of B14-65666. The deconvolved size is  $(0''.72 \pm 0''.20) \times (0''.15 \pm 0''.01)$ , indicating the spatially extended dust emission. Such an extended dust emission is also found in other  $z > 7$  galaxies with dust continuum detections; A1689-zD1 (Knudsen et al. 2017) and MACS0416\_Y1 (Y. Tamura et al. in prep).

The bottom right panel of Figure 2 shows contours of *dust90* overlaid on the F140W image. Although we see a tentative signal ( $3\sigma$ ) at the position of “clump B”, we reserve claiming this as a detection because of its low significance. We estimate the  $3\sigma$  upper limit of the flux density at 90  $\mu\text{m}$  using the spatial size of dust continuum at 163  $\mu\text{m}$  which corresponds to  $\approx 4$  beams in 90  $\mu\text{m}$ . We obtain a  $3\sigma$  upper limit of  $S_{\nu,90\mu\text{m}} < 370 \mu\text{Jy}$  ( $\approx 62.4 \mu\text{Jy} \times 3 \times \sqrt{4}$ ).

We estimate the total infrared luminosity by integrating the modified-black body radiation over  $8 - 1000 \mu\text{m}$ . Based on the  $3\sigma$  upper limit of the continuum ratio  $S_{\nu,90\mu\text{m}}/S_{\nu,163\mu\text{m}}$  and assuming the emissivity index of  $\beta_d = 1.5$  (e.g., Chapman et al. 2005; Casey 2012), we obtain the dust temperature upper limit to be  $T_d < 60 \text{ K}$ . At  $z = 7.1520$ , the temperature of the cosmic microwave background (CMB) is  $\approx 22 \text{ K}$ . Therefore, in this

<sup>8</sup> We have checked and confirmed that the flux density obtained from aperture photometry is consistent with the `imfit` result.

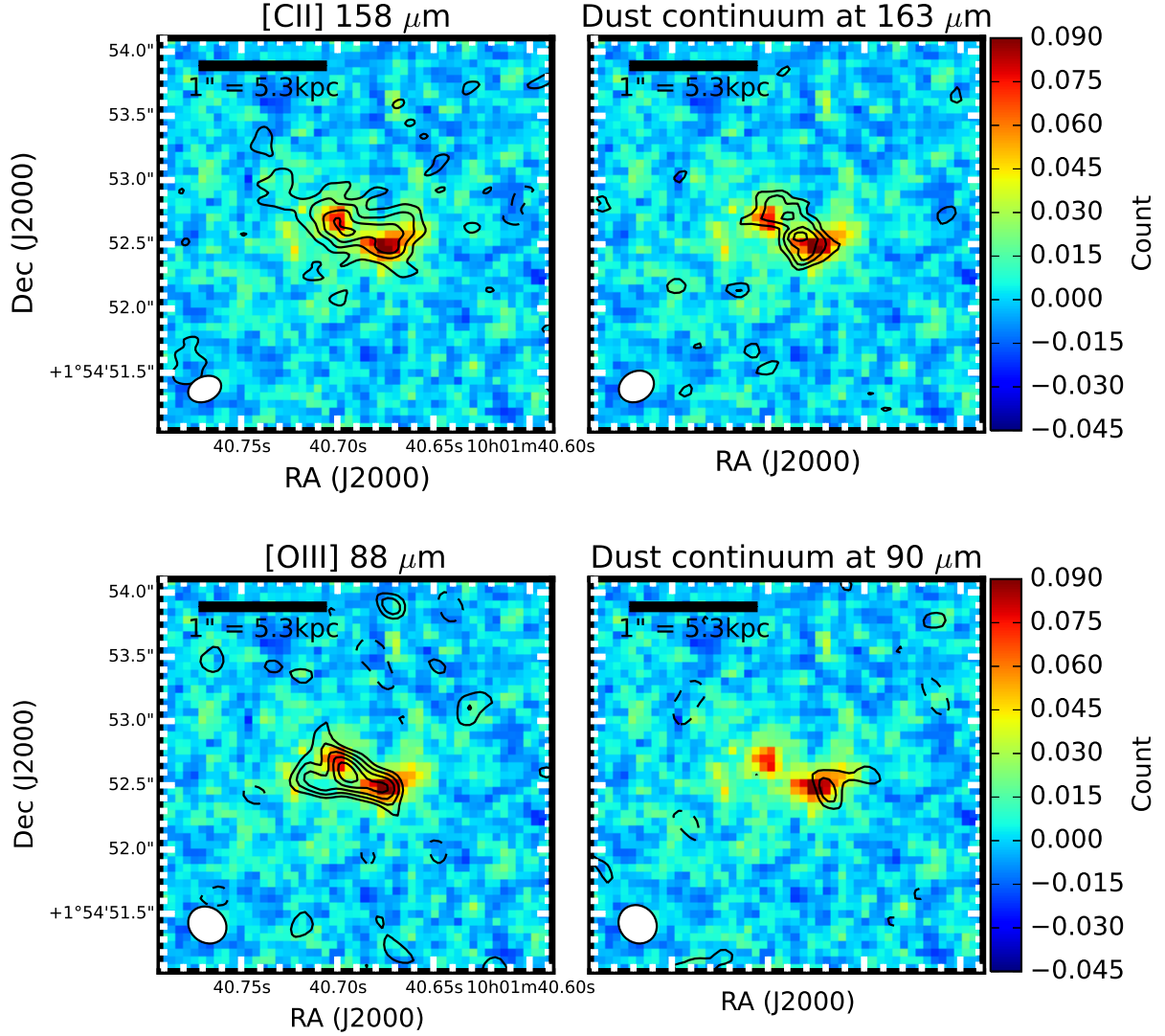


**Fig. 2.** Top and bottom panels show ALMA Band 6 and 8 data overlaid on the HST F140W image, respectively. (*Top Left*) [CII] line contours drawn at  $(-2, 2, 4, 6, 8) \times \sigma$ , where  $\sigma = 21 \text{ mJy beam}^{-1} \text{ km s}^{-1}$ . (*Top Right*) Dust continuum contours at  $\approx 163 \mu\text{m}$  drawn at  $(-2, 2, 3, 4, 5) \times \sigma$ , where  $\sigma = 9.5 \mu\text{Jy beam}^{-1}$ . (*Bottom Left*) [OIII] line contours drawn at  $(-2, 2, 3, 4, 5, 6) \times \sigma$ , where  $\sigma = 81 \text{ mJy beam}^{-1} \text{ km s}^{-1}$ . (*Bottom Right*) Dust continuum contours at  $\approx 90 \mu\text{m}$  drawn at  $(-2, 2, 3) \times \sigma$ , where  $\sigma = 62.4 \mu\text{Jy beam}^{-1}$ . In each panel, negative and positive contours are shown by the dashed and solid lines, respectively, and the ellipse at lower left indicates the synthesized beam size of ALMA.

**Table 4.** Line redshift for the two components

Parameters	clump A (North-East, redshifted)	clump B (South-West, blue-shifted)	Total
$z_{[\text{CII}]}$	$7.1535 \pm 0.0004$	$7.1483 \pm 0.0006$	$7.1521 \pm 0.0004$
$z_{[\text{OIII}]}$	$7.1527 \pm 0.0010$	$7.1483 \pm 0.0004$	$7.1510 \pm 0.0009$

Note. The clump A and clump B show a velocity offset of  $192 \pm 24 \text{ km s}^{-1}$  ( $162 \pm 40 \text{ km s}^{-1}$ ) in [CII] ([OIII]).

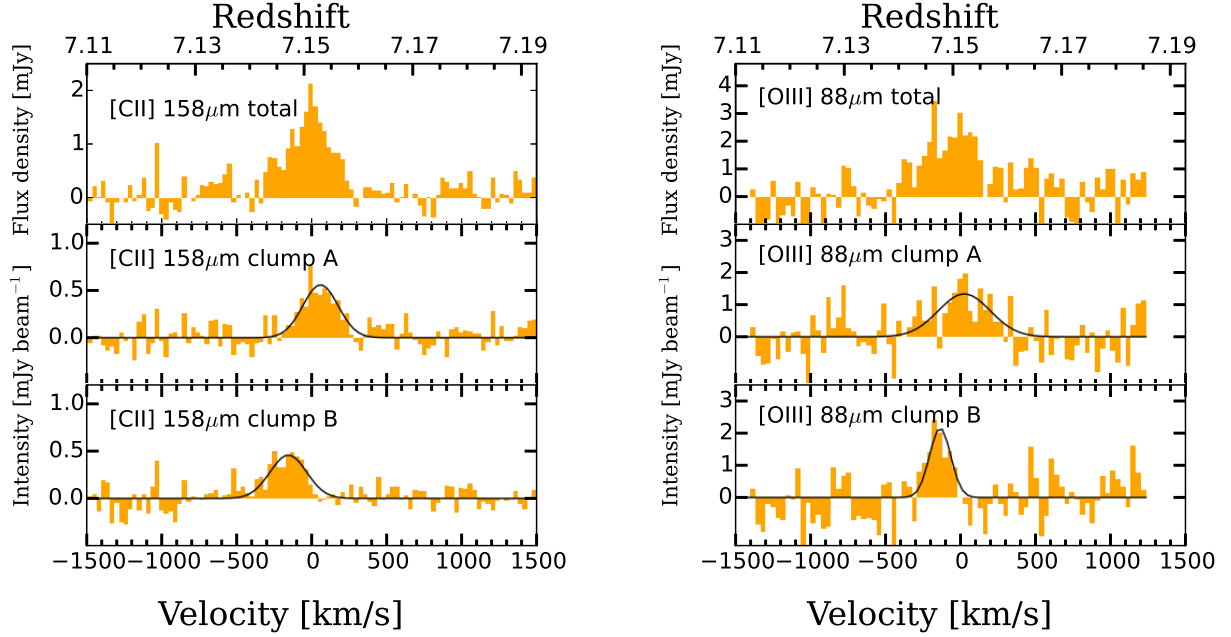


**Fig. 3.** (Left) Top panel shows the [CII] spectrum in units of mJy extracted from the region with  $> 3\sigma$  detections in the velocity-integrated intensity image. Middle and bottom panels show the [CII] spectra in units of mJy beam $^{-1}$  extracted from the two HST peaks indicated by crosses in Figure 4. The black line denotes the best-fit Gaussian for the line. (Right) The same as the left panel, but for [OIII].

study, we use dust temperatures of  $T_d = 30, 40$ , and  $50$  K and assume the emissivity index of  $\beta_d = 1.5$ . Similar values have been used in previous studies of high- $z$  star forming galaxies (Ouchi et al. 2013; Schaerer et al. 2015; Inoue et al. 2016) and determined in a  $z \approx 7.5$  galaxy (Knudsen et al. 2017). Correcting the CMB effects (da Cunha et al. 2013; Ota et al. 2014), we obtain the total infrared luminosity of  $L_{\text{TIR}} = (1.7 - 6.2) \times 10^{11} L_\odot$ . We find that  $L_{\text{TIR}}$  increases by a factor of  $1.0 - 1.3$  for the CMB effects at  $T_d = 30 - 50$  K. These values are summarized in Table 5. Our  $L_{\text{TIR}}$  is similar to the value in A1689-zD1 after the lensing correction (Knudsen et al. 2017).

Assuming a dust mass absorption coefficient  $\kappa = \kappa_0(\nu/\nu_0)^{\beta_d}$ , where  $\kappa_0 = 10 \text{ cm}^2 \text{ g}^{-1}$  at  $250 \mu\text{m}$  (Hildebrand 1983), we obtain the dust mass  $(1.2 - 5.6) \times 10^7 M_\odot$  (Table 5). If we use a dust mass absorption coefficient with  $\kappa_0 = 0.77 \text{ cm}^2 \text{ g}^{-1}$  at  $850 \mu\text{m}$  (Dunne et al. 2000), the dust mass estimates become twice as large.

## 5 Luminosity Ratios

### 5.1 IR-to-UV luminosity ratio (IRX) and IRX- $\beta$ relation

The relation between the IR-to-UV luminosity ratio,  $\text{IRX} \equiv \log_{10}(L_{\text{TIR}}/L_{\text{UV}})$ , and the UV continuum slope,  $\beta$ , is useful to constrain the dust attenuation curve of galaxies (e.g., Meurer et al. 1999). Local starburst galaxies are known to follow the Calzetti's curve (e.g., Calzetti et al. 2000; Takeuchi et al. 2012). Studies have shown that high- $z$  galaxies may favor a steep at-

**Table 5.** Dust properties.

$T_d$ (K)	$\beta_d$	$L_{\text{TIR}}$ ( $10^{11} L_\odot$ )	$M_d$ ( $10^7 M_\odot$ )
30	1.5	$1.7 \pm 0.3$	$5.6 \pm 1.1$
40	1.5	$3.2 \pm 0.6$	$2.2 \pm 0.4$
50	1.5	$6.2 \pm 1.2$	$1.2 \pm 0.2$

Note. The total luminosity,  $L_{\text{TIR}}$ , is estimated by integrating the modified-black body radiation at  $8 - 1000 \mu\text{m}$ . We use dust temperatures ranging from  $T_d = 30$  K to  $50$  K and the emissivity index  $\beta_d = 1.5$ . The dust mass,  $M_d$ , is estimated with a dust mass absorption coefficient  $\kappa = \kappa_0(\mu/\nu_0)^{\beta_d}$ , where we assume  $\kappa_0 = 10 \text{ cm}^2 \text{ g}^{-1}$  at  $250 \mu\text{m}$  (Hildebrand 1983).

tenuation curve similar to that of the Small Magellanic Cloud (SMC) (e.g., Reddy et al. 2006). Based on a stacking analysis of LBGs at  $z \approx 2 - 10$ , Bouwens et al. (2016) show that high- $z$  galaxies have a low IRX value at a given  $\beta$ , even lower than the SMC curve. This is interpreted as a steep attenuation curve or a high  $T_d$  at high- $z$ , the latter being supported from detailed analyses of the IR spectral energy distribution in high- $z$  analogs (Faisst et al. 2017). On the other hand, several studies claim that there is no or little redshift evolution in the IRX- $\beta$  relation at least up to  $z \approx 5$  (Fudamoto et al. 2017; Koprowski et al. 2018). Thus, a consensus is yet to be reached on the high- $z$  IRX- $\beta$  relation.

At  $z \gtrsim 6$ , little is understood about the IRX- $\beta$  relation due to the small sample with dust continuum detections (Bowler et al. 2018). Therefore, B14-65666 would provide us with a clue to understand the IRX- $\beta$  relation at  $z > 6$ . Bowler et al.

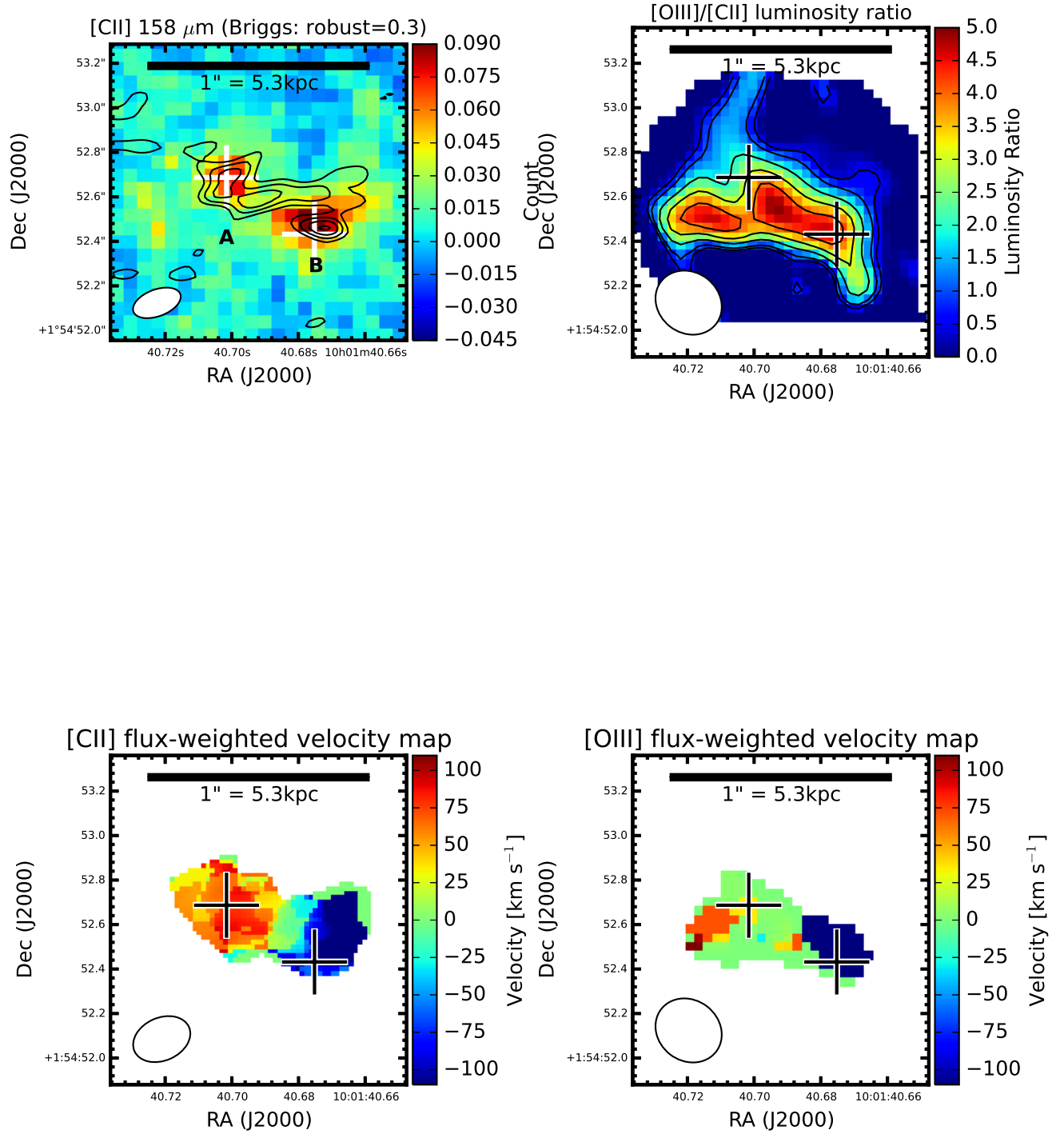


**Fig. 4.** (Top Left) Zoomed-in [CII] line image with a Briggs weighting (robust = 0.3). Contours are drawn at  $(-3, 2, 3, 4, 5) \times \sigma$ , where  $\sigma = 26 \text{ mJy beam}^{-1} \text{ km s}^{-1}$ . White crosses show two HST peaks. (Top Right) Line luminosity ratio map. Only data points around B14-65666 is shown. Contours are drawn at the line luminosity ratio  $[\text{OIII}]/[\text{CII}] = 0.5, 1.0, 2.0, 3.0, \text{ and } 4.0$ . (Bottom) Left and right panels show flux-weighted velocity (i.e., Moment 1) maps of [CII] and [OIII] lines, respectively. The velocity zero point is defined as the systemic redshift, 7.1520. Only pixels with detections above  $3\sigma$  are used to create the maps.

(2018) have first discussed the position of B14-65666 in the IRX- $\beta$  relation. The authors have compared B14-65666 with the  $z \approx 3 - 5$  results (Fudamoto et al. 2017; Koprowski et al. 2018), a stacking result of  $z \approx 4 - 10$  (Bouwens et al. 2016), and with another  $z > 7$  galaxy that has a dust continuum detection, A1689\_zD1 (Watson et al. 2015; Knudsen et al. 2017).

In this study, we focus on the IRX- $\beta$  relation at  $z > 6.5$  based on a compiled sample of 10 spectroscopically confirmed galaxies. Tables 6 and 7 summarize our sample from the literature and this study. The sample includes four galaxies with dust continuum detections: A1689\_zD1 (Watson et al. 2015; Knudsen et al. 2017), A2744\_YD4 (Laporte et al. 2017), MACS0416\_Y1 (Y. Tamura et al. in prepration), and B14-65666 (see also Bowler et al. 2018). In addition, the sample includes objects with deep  $3\sigma$  upper limits on the IRX obtained with ALMA: Himiko (Ouchi et al. 2013; Schaerer et al. 2015), IOK-1 (Ota et al. 2014; Schaerer et al. 2015), SXDF-NB1006-2 (Inoue et al. 2016), COS-301855981, COS-29870300247 (Smit et al. 2018), and MACS1149-JD1 (Hashimoto et al. 2018).

For fair comparisons of the data points, we uniformly derive  $\beta$  from two photometry values following the equation (1) of Ono et al. (2010). We use the combination of (F125W, F160W) and (F140W, F160W) at two redshift bins of  $z = 6.60 - 7.21$  and  $z = 7.5 - 9.11$ , respectively. These wavebands probe the rest-frame wavelength ranges of  $\approx 1600 - 2000 \text{ \AA}$  and  $1500 - 1700 \text{ \AA}$  at two redshift bins. Because of the difference in the probed wavelength range, the derived  $\beta$  values should be treated with caution. The estimated  $\beta$  values are summarized in Table 6. To estimate the UV luminosity,  $L_{UV}$ , we consistently use the rest-frame  $\approx 1500 \text{ \AA}$  magnitude of the waveband1 in Table 6. We have uniformly estimated the  $L_{TIR}$  value of the literature sample in the same manner as in §4 assuming  $T_d = 40$  or  $50 \text{ K}$  and  $\beta_d = 1.5$  as shown in Table 7.

Figure 5 shows the  $z > 6.5$  galaxies in the IRX- $\beta$  relation. We also plot the IRX- $\beta$  relations based on the Calzetti and SMC dust laws assuming the intrinsic  $\beta$  value of  $-2.2$  (Bouwens et al. 2016). We find that four LBGs with dust continuum detections are consistent with the Calzetti's curve if we assume  $T_d = 40$  or  $50 \text{ K}$ . Among the six null-detections, SXDF-NB1006-2 has a very steep UV slope  $\beta < -2.6$  ( $3\sigma$ ). Such a steep  $\beta$  can be reproduced if we assume a very young stellar age ( $< 10 \text{ Myr}$ ) or low metallicity (e.g., Schaerer 2003; Bouwens et al. 2010, see also Figure 10 of Hashimoto et al. 2017a). Likewise, MACS1149-JD1 has a stringent upper limit on the IRX value. Although it is possible that MACS1149-JD1 lies below the SMC curve, we note that the presented  $\beta$  value of MACS1149-JD1 probes the rest-frame wavelength range of  $1400 - 1600 \text{ \AA}$ . Deeper  $K$  band data would allow us to compute  $\beta$  in the wavelength range of  $\approx 1500 - 2200 \text{ \AA}$  which is comparable to that probed in previous high- $z$  studies (e.g., Bouwens et al. 2009; Hashimoto et al. 2017b).

Although a large and uniform sample with dust continuum detections is needed to understand the typical attenuation curve at  $z > 6.5$ , our first results show that there is no strong evidence for a steep (i.e., SMC-like) attenuation curve at least for the four LBGs detected in dust.

## 5.2 [OIII]/[CII] Luminosity Ratio

The line luminosity ratio, [OIII]/[CII], would give us invaluable information on chemical and ionization properties of galaxies (e.g., Inoue et al. 2014b; Marrone et al. 2018). For example, in local galaxies, a number of studies have examined the line ratio (Malhotra et al. 2001; Brauher et al. 2008; Madden et al. 2012; Cormier et al. 2015). These studies have shown that dwarf metal-poor galaxies have high line ratios, [OIII]/[CII]  $\approx 2 - 10$ , whereas metal-rich galaxies have low line ratios, [OIII]/[CII]  $\approx 0.5$ . Alternatively, if the ISM of galaxies is highly ionized, the [CII] luminosity would be weakened because [CII] emission is predominantly emitted from the PDR (e.g., Vallini et al. 2015; Katz et al. 2017).

In B14-65666, the total line luminosity ratio is [OIII]/[CII]  $= 2.2 \pm 0.4$ . We compare our results with those in other high- $z$  galaxies in the literature: two  $z \approx 7$  star-forming galaxies and a  $z = 6.90$  sub-millimeter galaxy (SMG). Inoue et al. (2016) have detected [OIII] from a  $z = 7.21$  LAE with the  $EW_0(\text{Ly}\alpha)$  value of  $33 \text{ \AA}$  (SXDF-NB1006-2; Shibuya et al. 2012). With the null detection of [CII], the authors have shown that SXDF-NB1006-2 has a total line luminosity ratio of [OIII]/[CII]  $> 12$  ( $3\sigma$ ). Carniani et al. (2017a) have reported detections of [OIII] and [CII] in a galaxy at  $z = 7.11$  (BDF-3299; Vanzella et al. 2011; Maiolino et al. 2015). BDF-3299 has a large  $EW_0(\text{Ly}\alpha) = 50 \text{ \AA}$  and thus can be categorized into LAEs. The galaxy has spatial offsets between [OIII], [CII], and UV emission. Under the assumption that both [CII] and [OIII] are associated with the UV emission, we obtain the total line ratio of  $3.7 \pm 0.6$  using the [CII] luminosity ( $4.9 \pm 0.6 \times 10^8 L_\odot$ ) and the [OIII] luminosity ( $18 \pm 2 \times 10^8 L_\odot$ )<sup>9</sup>. Recently, Marrone et al. (2018) have detected both [OIII] and [CII] from a lensed SMG at  $z = 6.90$  comprised of two galaxies (SPT0311-058E and SPT0311-058W). The total line luminosity ratio is  $1.27 \pm 0.18$  and  $0.56 \pm 0.17$  for SPT0311-058E and SPT0311-058W, respectively, where the  $1\sigma$  values take the uncertainties on magnification factors into account.

Based on the combined sample of these literature objects with B14-65666, we investigate the relation between the line luminosity ratio and the bolometric luminosity estimated as  $L_{bol} \approx L_{UV} + L_{TIR}$ . For the two LAEs without dust continuum detections, we derive the upper limits of  $L_{bol}$  as the  $L_{UV}$  mea-

<sup>9</sup> Carniani et al. (2017a) have obtained the line ratio at the [OIII] emitting region without [CII] emission  $> 8$  at  $5\sigma$ . Because the value is obtained in a partial region of the galaxy, we have computed the total line luminosity ratio for fair comparisons to other data points.

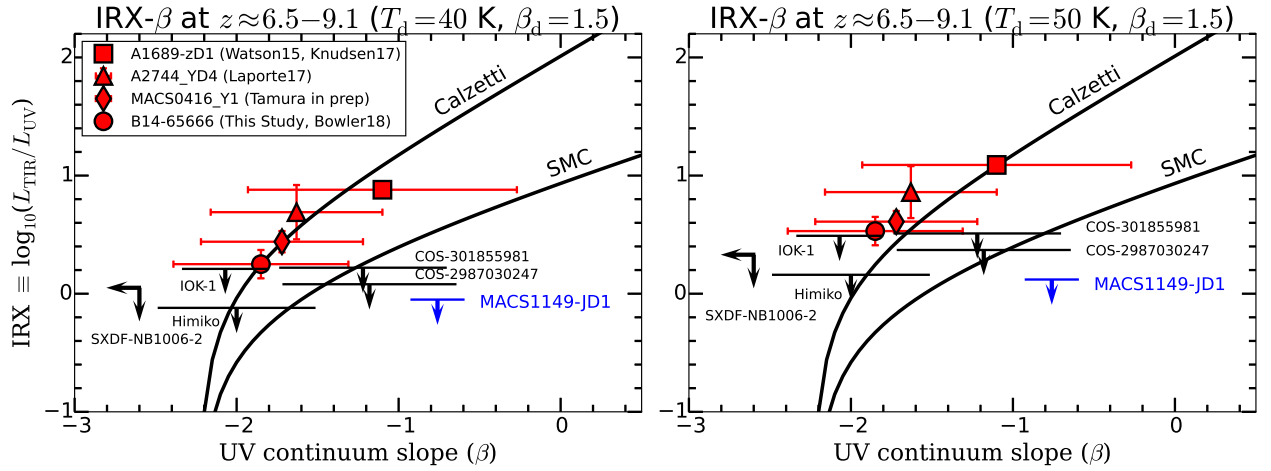


**Fig. 5.** The IRX, plotted against the UV slope,  $\beta$ , for 10 spectroscopically identified galaxies at  $z \approx 6.5 - 9.1$ . In the left (right) panel, we plot the IRX value under the assumption of  $T_d = 40$  (50) K and  $\beta_d = 1.5$ . For fair comparisons of data points, we have uniformly derived  $\beta$  and IRX values (see §5.1 for the details). In each panel, the two solid black lines indicate the iRX- $\beta$  relation based on the Calzetti and SMC dust laws (Bouwens et al. 2016). The four red symbols denote objects with dust continuum detections; A1689\_zD1 (Watson et al. 2015; Knudsen et al. 2017), A2744\_YD4 (Laporte et al. 2017), MACS0416\_Y1 (Y. Tamura et al. in preparation), and B14-65666. The details of the data are summarized in Tables 6 and 7.

**Table 6.** The ALMA spectroscopic literature sample: UV continuum slopes

Name (1)	Redshift (2)	Waveband1 (3)	Waveband2 (4)	$\lambda_{\text{rest}}$ (5) (Å)	$\beta$ (6)	$L_{\text{UV}}$ (7) ( $10^{10} L_{\odot}$ )	$\mu$ (8)
MACS1149-JD1	9.11	F140W = $25.88 \pm 0.02$	F160W = $25.70 \pm 0.01$	1400 – 1600	$-0.76 \pm 0.16$	$(8.6 \pm 0.2)/\mu$	10
A2744_YD4	8.38	F140W = $26.46 \pm 0.04$	F160W = $26.42 \pm 0.04$	1500 – 1700	$-1.63 \pm 0.53$	$(4.5 \pm 0.2)/\mu$	$1.8 \pm 0.3$
MACS0416_Y1	8.31	F140W = $26.08 \pm 0.05$	F160W = $26.04 \pm 0.05$	1500 – 1700	$-1.72 \pm 0.50$	$(6.3 \pm 0.3)/\mu$	1.4
A1689_zD1	7.5	F140W = $24.64 \pm 0.05$	F160W = $24.51 \pm 0.11$	1600 – 1900	$-1.10 \pm 0.83$	$(20.5 \pm 0.9)/\mu$	9.3
SXDF-NB1006-2	7.21	$J = 25.46 \pm 0.18$	$H > 25.64 (3\sigma)$	1500 – 1900	$< -2.6 (3\sigma)$	$9.1 \pm 1.5$	—
B14-65666	7.15	$J = 24.7^{+0.2}_{-0.2}$	$H = 24.6^{+0.3}_{-0.2}$	1500 – 1900	$-1.85^{+0.54}_{-0.53} a$	$18.1 \pm 3.4$	—
IOK-1	6.96	F125W = $25.42 \pm 0.05$	F160W = $25.44 \pm 0.06$	1600 – 2000	$-2.07 \pm 0.26$	$9.0 \pm 0.4$	—
COS-301855981	6.85	F125W $-^b$	F160W $-^b$	1600 – 2000	$-1.22 \pm 0.51$	$11 \pm 1^c$	—
COS-2987030247	6.81	F125W $-^b$	F160W $-^b$	1600 – 2000	$-1.18 \pm 0.53$	$13 \pm 1^c$	—
Himiko	6.60	F125W = $24.99 \pm 0.08$	F160W = $24.99 \pm 0.10$	1600 – 2100	$-2.00 \pm 0.48$	$12.4 \pm 1.1$	—

Note. (1) Object Name; (2) Spectroscopic redshift; (3) and (4) Two wavebands and their photometry values to derive the UV continuum slope; (5) Rest-frame wavelength range probed by the wavebands; (6) UV spectral slope; (7) UV luminosity at  $\approx 1500$  Å obtained from the photometry value of the Waveband1; and (8) lensing magnification factor.

Redshift and photometry values are taken from the literature as summarized below.

MACS1149-JD1: Redshift (Hashimoto et al. 2018); F140W and F160W (Zheng et al. 2017);

A2744\_YD4: Redshift (Laporte et al. 2017); F140W and F160W (Zheng et al. 2014);

MACS0416\_Y1: Redshift (Y. Tamura et al. in prep.); F140W and F160W (Laporte et al. 2015);

A1689\_zD1: Redshift (Watson et al. 2015); F125W and F160W (Watson et al. 2015);

SXDF-NB1006-2: Redshift (Inoue et al. 2016);  $J$  and  $H$  (Inoue et al. 2016);

B14-65666: Redshift (This Study);  $J$  and  $H$  (Bowler et al. 2014);

IOK-1: Redshift (Ota et al. 2014); F125W and F160W (Jiang et al. 2013; the object No. 62 in their Table 1);

Himiko: Redshift (Ouchi et al. 2013); F125W and F160W (Ouchi et al. 2013)

<sup>a</sup> The UV spectral slope in Bowler et al. (2018) based on the latest photometry value is presented.

<sup>b</sup> Not available.

<sup>c</sup> Values taken from Smit et al. (2018).

**Table 7.** The ALMA spectroscopic literature sample: Infrared-excess (IRX)

Name	$S_\nu$ ( $\mu\text{Jy}$ )	Rest-Wavelength ( $\mu\text{m}$ )	$L_{\text{TIR}40}$ ( $10^{10} L_\odot$ )	$L_{\text{TIR}50}$ ( $10^{10} L_\odot$ )	IRX <sub>40</sub>	IRX <sub>50</sub>	Ref.
(1)	(2)	(3)	(4)	(5)	(6)	(7)	(8)
MACS1149-JD1	$< 53/\mu (3\sigma)$	90	$< 7.7/\mu$	$< 11.4/\mu$	$< -0.05$	$< 0.12$	Hashimoto et al. (2018)
A2744_YD4	$(175 \pm 69)/\mu^a$	90	$(22.0 \pm 8.7)/\mu$	$(32.7 \pm 12.9)/\mu$	$0.69 \pm 0.23$	$0.86 \pm 0.22$	Laporte et al. (2017)
MACS0416_Y1	$(137 \pm 26)/\mu$	91	$(17.2 \pm 3.3)/\mu$	$(25.7 \pm 4.9)/\mu$	$0.44 \pm 0.09$	$0.61 \pm 0.09$	Y. Tamura et al. in prep.
A1689_zD1	$(1330 \pm 140)/\mu$	103	$(157 \pm 16.6)/\mu$	$(255 \pm 26.8)/\mu$	$0.88 \pm 0.05$	$1.09 \pm 0.05$	Knudsen et al. (2017)
SXDF-NB1006-2	$< 42 (3\sigma)$	162	$< 10.2$	$< 19.6$	$< 0.05$	$< 0.33$	Inoue et al. (2016)
B14-65666	$130 \pm 25$	163	$32.0 \pm 6.1$	$61.8 \pm 11.9$	$0.25 \pm 0.12$	$0.53 \pm 0.12$	Bowler et al. (2018), This Study
IOK-1	$< 63 (3\sigma)$	162	$< 14.5$	$< 28.0$	$< 0.21$	$< 0.49$	Ota et al. (2014)
COS-3018555981	$< 87 (3\sigma)$	158	$< 18.3$	$< 35.4$	$< 0.22$	$< 0.51$	Smit et al. (2018)
COS-2987030247	$< 75 (3\sigma)$	158	$< 15.6$	$< 30.2$	$< 0.08$	$< 0.37$	Smit et al. (2018)
Himiko	$< 51 (3\sigma)$	153	$< 9.3$	$< 18.0$	$< -0.12$	$< 0.16$	Ouchi et al. (2013)

Note. (1) Object Name; (2) and (3) Dust continuum flux density and its rest-frame wavelength; (4) and (5) Total IR luminosities estimated by integrating the modified-black body radiation at  $8 - 1000 \mu\text{m}$  with  $T_d = 40 \text{ K}$  and  $50 \text{ K}$ , respectively, and  $\beta_d = 1.5$ ; (6) and (7) IRX values at  $T_d = 40 \text{ K}$  and  $50 \text{ K}$ , respectively; and (8) Reference. Upper limits represent  $3\sigma$ .

<sup>a</sup> Continuum flux density after performing primary beam correction.

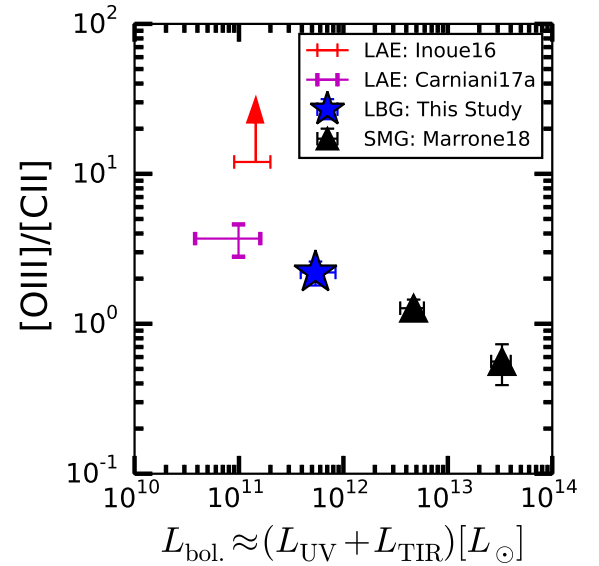
surements plus the  $3\sigma$  upper limits of  $L_{\text{TIR}}$ , where we assume  $T_d = 40 \text{ K}$  and  $\beta_d = 1.5$ . The  $L_{\text{UV}}$  value is used as lower limits of  $L_{\text{bol}}$ . In our LBG, we use  $T_d = 40 \pm 10 \text{ K}$  to compute  $L_{\text{TIR}}$  and add its uncertainty to the  $1\sigma$  value of  $L_{\text{bol}}$ . The  $L_{\text{TIR}}$  value of the two SMGs are well constrained from multiple dust continuum detections at different wavelengths (see Extended Data Figure 7 in Marrone et al. 2018). Because these SMGs have  $L_{\text{UV}}/L_{\text{TIR}} \approx 0.002 - 0.02$ , we assume  $L_{\text{bol}} \approx L_{\text{TIR}}$  for these objects.

Figure 6 shows a clear anti-correlation, although a larger number of galaxies are needed for a definitive conclusion. Given that the bolometric luminosity traces the mass scale of a galaxy (i.e., the stellar and dark matter halo masses and/or the SFR), the possible trend implies that lower mass galaxies having higher luminosity ratios. These would in turn indicate that lower mass galaxies have either lower metallicity or higher ionization states (cf., Nakajima et al. 2016). The results remain unchanged if we assume  $T_d = 30$  or  $50 \text{ K}$  to obtain  $L_{\text{TIR}}$  for LAEs.

Because the [CII] and [OIII] lines of B14-65666 are spatially resolved, we also create the map of the line luminosity ratio (see Marrone et al. 2018). To do so, we first match the beam size and position angle of [CII] data to those of [OIII] with the CASA task `imsmooth`. We then use the CASA task `immath` to create a line luminosity ratio map taking into account the difference in the observed frequencies (see equation (1)). The top right panel of Figure 4 shows that the line luminosity ratio is high in the central part of B14-65666.

### 5.3 Line-to-IR Luminosity Ratio

It is widely known that the luminosity ratio  $L_{[\text{CII}]} / L_{\text{TIR}}$  becomes smaller for galaxies with larger  $L_{\text{TIR}}$ , the so-called FIR line deficit (e.g., Brauer et al. 2008; Graciá-Carpio et al. 2011;



**Fig. 6.** [OIII]-to-[CII] line luminosity ratio plotted against the bolometric luminosity estimated as the summation of the UV and IR luminosities for  $z \approx 6 - 7$  objects. In B14-65666 (a blue five-pointed star), the horizontal error bar includes the uncertainty on  $T_d = 40 \pm 10 \text{ K}$ . The red arrow represents the  $3\sigma$  lower limit of the line luminosity ratio in the LAE of Inoue et al. (2016). For the two LAEs without  $L_{\text{TIR}}$  measurements, the upper limits of  $L_{\text{bol}}$  are estimated as the summation of  $L_{\text{UV}}$  and the  $3\sigma$  upper limits on  $L_{\text{TIR}}$ , where we assume  $T_d = 40 \text{ K}$  and  $\beta_d = 1.5$ . The lower limits of  $L_{\text{bol}}$  for the two LAEs correspond to  $L_{\text{UV}}$ .

Díaz-Santos et al. 2013). Based on the line luminosities (Table 3) and the total infrared luminosity (Table 5), we obtain the luminosity ratio  $\log(L_{\text{[CII]}}/L_{\text{TIR}}) = -2.1 \pm 0.1$ ,  $-2.4 \pm 0.1$ , and  $-2.7 \pm 0.1$ , for  $T_d = 30, 40$ , and  $50$  K, respectively. The range is well consistent with local observations (e.g., Díaz-Santos et al. 2013) and high- $z$  observations including normal star-forming galaxies (Capak et al. 2015) as well as QSO host galaxies (e.g., Venemans et al. 2017; Izumi et al. 2018). Izumi et al. (2018) have argued a possibility that  $z \gtrsim 6$  objects have higher luminosity ratios than local objects. Due to the large uncertainty in our  $L_{\text{TIR}}$  estimate, we cannot investigate if the trend is true for B14-65666.

## 6 SED fit

We perform stellar population synthesis model fitting to B14-65666 to derive the stellar mass ( $M_*$ ), dust attenuation ( $A_V$ ), the stellar age, stellar metallicity ( $Z$ ), and the SFR. In this section, we first perform SED fitting with single stellar component models. We demonstrate that such models have a difficulty in reproducing the dust mass of B14-65666 (§6.1). We then show how two-component SED models are necessary to reproduce the estimated dust mass with a reasonable stellar age (§6.2).

We use the  $Y$ ,  $J$ ,  $H$ , and  $K$  band data taken by UltraVISTA (Bowler et al. 2014) and the deep *Spitzer*/IRAC 3.6 and  $4.5 \mu\text{m}$  data (Bowler et al. 2017). Specifically, we have used the latest photometry values in Bowler et al. (2018). The clumps A and B in Figure 4 are not resolved under the coarse angular resolution of ground based telescopes. Therefore, the photometry values represent the total system of B14-65666. We thus perform SED fitting to the total system. In addition, we use our measurement ( $163 \mu\text{m}$ ) and upper limit ( $90 \mu\text{m}$ ) on dust continuum emission as well as our measurement of the [OIII] flux. We do not use the [CII] flux. This is due to the difficulty in modeling [CII] which arises both from the HII region and the PDR (see Inoue et al. 2014b).

The SED fitting code used in this study is the same as that used in Hashimoto et al. (2018). For the detailed procedure, we refer the reader to Mawatari et al. (2016) and the relevant link <sup>10</sup>. Briefly, the stellar population synthesis model of GALAXEV (Bruzual & Charlot 2003) is used. The nebular continuum and emission lines of Inoue (2011a) are included. The [OIII] line flux is estimated based on metallicity and the SFR with semi-empirical models (Inoue et al. 2014b, 2016). A Calzetti's law (Calzetti et al. 2000) is assumed for dust attenuation. The same attenuation value is used for the stellar and nebular components (e.g., Erb et al. 2006; Kashino et al. 2013). An empirical dust emission templates of Rieke et al. (2009) is adopted. The Chabrier initial mass function (Chabrier 2003) with  $0.1 - 100 M_\odot$  is adopted, and a mean IGM model of Inoue et al. (2014a)

**Table 8.** Results of SED fit

One-component model	
Parameters	Values
$\chi^2$	6.97
$\nu$	4
$A_V$ [mag]	$0.20^{+0.16}_{-0.08}$
Age [Myr]	$5.0^{+1.3}_{-2.4}$
Metallicity	$0.004^{+0.012}_{-0.000}$
Escape fraction	$0.0^{+0.1}_{-0.0}$
Stellar mass ( $M_\odot$ ) [ $10^9 M_\odot$ ]	$0.64^{+0.14}_{-0.02}$
SFR [ $M_\odot \text{ yr}^{-1}$ ]	$129^{+91}_{-1}$
Two-component model	
$\chi^2$	5.85
$\nu$	6
$A_{V,\text{young}} = A_{V,\text{old}}$ [mag]	0.20 (fixed)
Metallicity <sub>young</sub> = Metallicity <sub>old</sub>	0.004 (fixed)
Age <sub>old</sub> [Myr]	200 (fixed)
Age <sub>young</sub> [Myr]	$3.8^{+2.4}_{-0.8}$
Escape fraction	0.0
$f_{\text{SFR0}} \equiv (\text{SFR}_{\text{old}}/\text{SFR}_{\text{young}})_{z=7.15}$	$0.079^{+0.091}_{-0.077}$
Total stellar mass ( $M_*$ ) [ $10^9 M_\odot$ ]	$2.1^{+1.1}_{-1.4}$
Total SFR [ $M_\odot \text{ yr}^{-1}$ ]	$143^{+15}_{-27}$

Note. The stellar mass and SFR values are obtained with the Chabrier IMF with  $0.1 - 100 M_\odot$ . In the one-component models, there is a problem that the stellar age is too small to reproduce the dust mass (see §6.1).

is applied. We fix the object's redshift of 7.1520. To estimate the best-fit parameters, we use the least  $\chi^2$  formula of Sawicki (2012) including an analytic treatment of upper limits for non-detections. Uncertainties on the parameters are estimated based on a Monte Carlo technique ( $N = 300$ ).

### 6.1 Single stellar component models and problems

For simplicity, we assume a constant star formation history (SFH). The panels (a) - (c) of Figure 7 show the best-fit SED of B14-65666 and the upper rows of Table 8 summarize the estimated physical quantities. The strong [OIII] line flux indicates a very large current SFR,  $129^{+91}_{-1} M_\odot \text{ yr}^{-1}$ . We note that our stellar mass,  $M_* = 6.4^{+1.4}_{-0.2} \times 10^8 M_\odot$ , or  $\log(M_*/M_\odot) = 8.8^{+0.1}_{-0.1}$ , is smaller than that obtained in Bowler et al. (2014) by a factor of two. This is because our SED fit code includes the contributions of nebular emission lines to the photometry, whereas that of Bowler et al. (2014) does not. Indeed, the IRAC  $4.5 \mu\text{m}$  band is boosted by strong [OIII]  $\lambda\lambda$  4959 Å and 5007 Å emission lines in the best-fit model.

The problem of single stellar component models is that the best-fit stellar age ( $\approx 5$  Myr) is too small to reproduce the dust mass as described below. Based on a combination of the stellar mass of  $\approx 6.4 \times 10^8 M_\odot$  (Table 5) and the effective number of supernovae (SN) per unit stellar mass in the Chabrier IMF,  $0.0159 M_\odot^{-1}$  (e.g., Inoue 2011b), we obtain the number of SN  $\approx 1 \times 10^7$ . Thus, the dust mass of  $\approx (1 - 6) \times 10^7 M_\odot$  requires

<sup>10</sup><https://www.astr.tohoku.ac.jp/~mawatari/KENSFIT/KENSFIT.html>

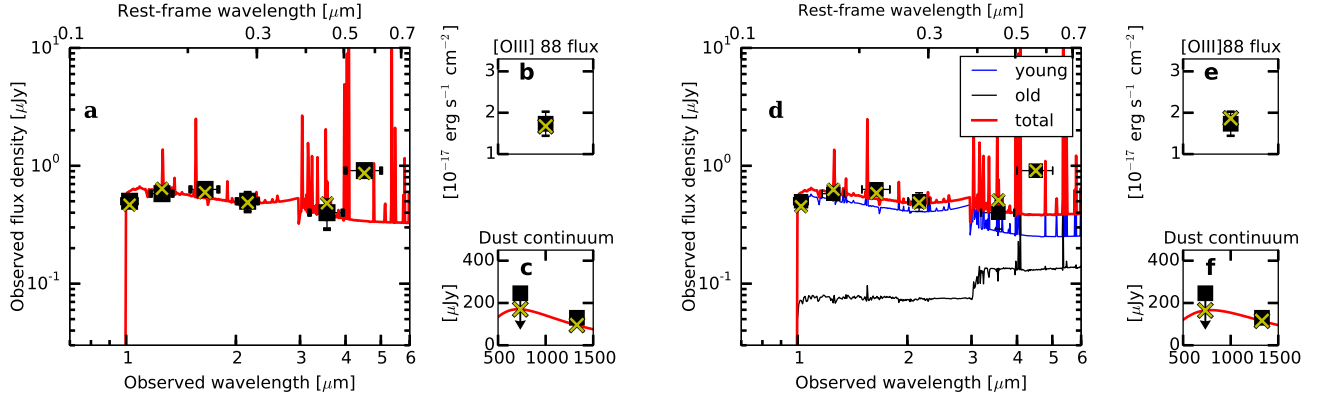


**Fig. 7.** (*Left*) Best-fit SED (panel a) taking into account the [OIII] flux (panel b) and the dust continuum flux density (panel c) for a single stellar component model. In panel (a), black squares show  $Y$ ,  $J$ ,  $H$ ,  $K$ -band photometry and the IRAC channel 1 and 2 measurements. Horizontal and vertical error bars represent the wavelength range of the filters and the  $1\sigma$  uncertainties, respectively. The red solid line indicates the SED model and the corresponding band flux densities are shown by yellow crosses. In panel (b), the black square shows the observed [OIII] flux and its  $1\sigma$  uncertainty, while the yellow cross is the model prediction. In panel (c), the black squares are the  $2\sigma$  upper limit at  $90\ \mu\text{m}$  and the dust emission measurement at  $163\ \mu\text{m}$ . (*Right*) The same for the left panel but for the two-component model. In panel (d), blue and black lines correspond to the contributions from the young and old component, respectively.

the dust yield per SN as large as  $\approx 1 - 6\ M_{\odot}$ . To achieve such a high dust yield, the dust destruction process cannot be at work and the ISM growth should be significant (e.g., Michałowski 2015). However, this is physically unlikely to happen within the short stellar age ( $\approx 5\ \text{Myr}$ ). Note that AGB stars cannot contribute to the dust mass either because the typical time scale for AGB stars to contribute to the dust mass is  $\gtrsim 100\ \text{Myr}$  (e.g., Valiante et al. 2009).

In summary, the single stellar population models can formally reproduce the observed SED, but the best-fit stellar age is physically unacceptable given the large dust mass. We have checked and confirmed that the estimated stellar age is similarly small if we use an exponentially declining or rising star formation history (SFH).

## 6.2 Two-component SED models

We note that the stellar age ( $\approx 5\ \text{Myr}$ ) deduced from the SED fitting indicates the age after the onset of current star formation activity. Given the signature of merger activity discussed in §3.1, we infer the existence of star formation activity well before the observing timing at  $z = 7.15$  which forms two galaxies and a significant fraction of the dust mass. Therefore, we introduce two-component SED models.

To do so, we consider a two-component SED comprising a young starburst ignited by the merger event and an old underlying population. For simplicity, we assume that the old component has a constant SFR for a duration of  $\tau = 200\ \text{Myr}$ . With  $\tau = 200\ \text{Myr}$ , the dust grain growth in the ISM and the contribution from AGB stars are expected to be at work. This can further reduce the dust yield per SN. We assume that the secondary starburst initiates immediately after the star formation duration of the old component. We also assume that the two

components have common dust attenuation and metallicity values estimated in §6.1. The free parameters are the stellar age of the young component,  $\text{Age}_{\text{young}}$ , the total SFR as an amplitude of the SED, and the SFR ratio between of the old and young components at  $z = 7.1520$ ,  $f_{\text{SFR}0} \equiv (\text{SFR}_{\text{old}}/\text{SFR}_{\text{young}})_{z=7.15}$ .

The panels (d) - (f) of Figure 7 show the two-component SED and the lower rows of Table 8 summarize the results. The observed SEDs are well reproduced with the two-component models. We find that the stellar mass is increased by a factor of three compared with that in §6.1. The dust-to-stellar mass ratio ranges from  $\log(M_*/M_d) = -2.3$  to  $-1.6$ . The mass ratio can be explained by theoretical models (Popping et al. 2017; Calura et al. 2017) which predict the mass ratio of  $\lesssim -1.6$  in the Chabrier IMF. In this case, the dust yield per SN becomes  $\approx 0.3 - 1.8$  for  $T_d = 30 - 50\ \text{K}$ . The inferred range of the dust yield per SN can be further reduced with the dust growth in the ISM (e.g., Michałowski 2015) or contributions from AGB stars (e.g., Valiante et al. 2009).

We stress that the motivation of our two-component SED models is not to obtain a unique solution of SFH of B14-65666, but to demonstrate that such models can reasonably explain the observed dust amount as well as the merger signature. We have checked different star-formation durations of the old component,  $\tau = 100$  and  $300\ \text{Myr}$ , also give similar solutions to those of  $\tau = 200\ \text{Myr}$  and do not change our conclusion. We adopt the results of the two-component SED models to discuss the properties of B14-65666.

## 7 Ly $\alpha$ velocity offset

Because Ly $\alpha$  is a resonant line, it is known that the Ly $\alpha$  redshift,  $z_{\text{Ly}\alpha}$ , does not exactly match the systemic redshift defined by optically-thin nebular emission lines, e.g., [OIII] and

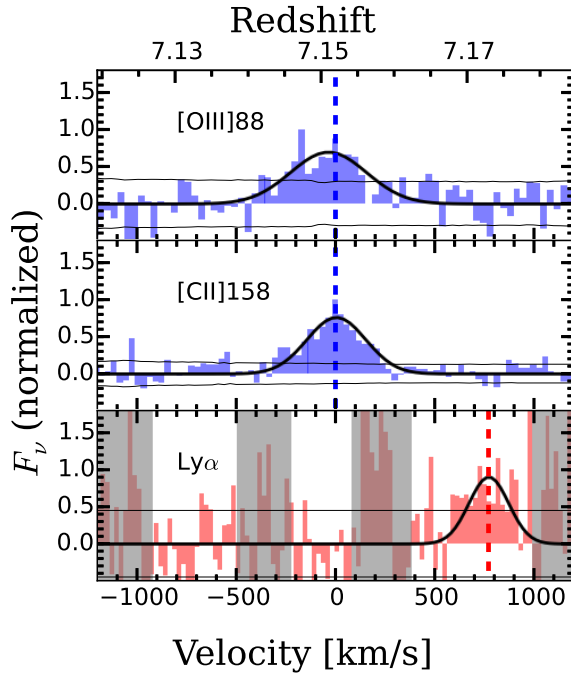


**Fig. 8.** Top, middle, and bottom panel show ALMA [OIII] 88  $\mu\text{m}$ , ALMA [CII] 158  $\mu\text{m}$ , and Subaru/FOCAS Ly $\alpha$  spectra in velocity space with a resolution of  $\sim 30 \text{ km s}^{-1}$ ,  $33 \text{ km s}^{-1}$ , and  $25 \text{ km s}^{-1}$ , respectively. The velocity zero point corresponds to the systemic redshift  $z = 7.1520$  (blue dashed line) and the Ly $\alpha$  offset is  $\simeq 770 \text{ km s}^{-1}$  (red dashed line). Grey rectangles show regions contaminated by night sky emission. The black solid lines indicate the RMS noise level for the velocity resolutions, and the black curves are Gaussian fit the lines.

[CII]. The discrepancy between the two redshifts provides a valuable probe of the interstellar medium (ISM) and the surrounding intergalactic medium (IGM). For example, based on radiative transfer calculations, theoretical studies (Dijkstra et al. 2006; Verhamme et al. 2006, 2015; Gronke et al. 2015) predict that the Ly $\alpha$  line is redshifted (blueshifted) with respect to the systemic redshift if a galaxy has an outflowing (inflowing) gas in the ISM. When Ly $\alpha$  photons enter the IGM, its spectral profile is further altered due to the damping wing of Ly $\alpha$  absorption by the intergalactic neutral hydrogen, increasing  $z_{\text{Ly}\alpha}$  (Haiman 2002; Laursen et al. 2013).

We measure the velocity offset of the Ly $\alpha$  line calculated as

$$\Delta v_{\text{Ly}\alpha} = c \times \frac{z_{\text{Ly}\alpha} - z_{\text{sys}}}{1 + z_{\text{sys}}}, \quad (2)$$

where  $c$  is the speed of light and  $z_{\text{sys}}$  is the systemic redshift. We define  $z_{\text{sys}}$  as the  $S/N$  weighted-mean redshift of the total [OIII] and [CII] lines,  $7.1520 \pm 0.0003$  (see Table 3). We have remeasured  $z_{\text{Ly}\alpha}$  in the spectrum of Furusawa et al. (2016), taking into account air refraction and the motion of the observatory. With the vacuum rest-frame wavelength of  $1215.67 \text{ \AA}$ , we have obtained  $z_{\text{Ly}\alpha} = 7.1730 \pm 0.0012$  in the Solar system barycentric frame (Table 3). Thus, we obtain  $\Delta v_{\text{Ly}\alpha} = 772 \pm 45 \text{ km s}^{-1}$  (Figure 8).

We compare the  $\Delta v_{\text{Ly}\alpha}$  value of B14-65666 with those in

the literature. The Ly $\alpha$  velocity offsets are investigated in hundreds of galaxies at  $z \approx 2 - 3$  where both Ly $\alpha$  and H $\alpha$  or [OIII] 5007  $\text{\AA}$  are available (e.g., Steidel et al. 2010; Hashimoto et al. 2013, 2015; Erb et al. 2014; Shibuya et al. 2014). At  $z \approx 2 - 3$ , galaxies have velocity offsets ranging from 100 to  $1000 \text{ km s}^{-1}$  with a mean value of  $200 - 400 \text{ km s}^{-1}$  (e.g., Erb et al. 2014; Trainor et al. 2015; Nakajima et al. 2018). At  $z > 6$ , there are 16 galaxies whose  $\Delta v_{\text{Ly}\alpha}$  values are measured. The systemic redshifts of these galaxies are based on either [CII] 158  $\mu\text{m}$  and [OIII] 88  $\mu\text{m}$  (Willott et al. 2015; Knudsen et al. 2016; Inoue et al. 2016; Pentericci et al. 2016; Bradač et al. 2017; Carniani et al. 2017a, 2018; Laporte et al. 2017; Matthee et al. 2017) or rest-frame UV emission lines such as CIII]1909 and OIII]1666 (Stark et al. 2015b, 2017; Mainali et al. 2017; Verhamme et al. 2018). At  $z \approx 6 - 8$ , velocity offsets of  $100 - 500 \text{ km s}^{-1}$  are reported. We summarize these literature sample at  $z \approx 6 - 8$  in Table 9. Compared with these literature values, the  $\Delta v_{\text{Ly}\alpha}$  value of B14-65666 is the largest at  $z \approx 6 - 8$ , and even larger than the typical  $\Delta v_{\text{Ly}\alpha}$  value at  $z \approx 2 - 3$ . This would be due to the fact that B14-65666 has a very bright magnitude of  $M_{\text{UV}} = -22.3$  and a small  $\text{EW}_0(\text{Ly}\alpha) = 3.7^{+1.7}_{-1.1} \text{ \AA}$ . Indeed, at  $z \approx 2 - 3$ , larger  $\Delta v_{\text{Ly}\alpha}$  values are found in galaxies with brighter  $M_{\text{UV}}$  (Erb et al. 2014) and smaller  $\text{EW}_0(\text{Ly}\alpha)$  (e.g., Hashimoto et al. 2013; Shibuya et al. 2014; Erb et al. 2014). The correlations between  $\Delta v_{\text{Ly}\alpha}$ ,  $M_{\text{UV}}$ , and  $\text{EW}_0(\text{Ly}\alpha)$  are theoretically explained as a result of radiative transfer effects. Brighter  $M_{\text{UV}}$  objects have larger neutral hydrogen column densities ( $N_{\text{HI}}$ ) in the ISM (Garel et al. 2012; Erb et al. 2014). In the case of large  $N_{\text{HI}}$ , the number of resonant scattering of Ly $\alpha$  photons becomes large. This in turn increases the  $\Delta v_{\text{Ly}\alpha}$  value and reduces the  $\text{EW}_0(\text{Ly}\alpha)$  value (e.g., Verhamme et al. 2015).

To better understand the origin of the large  $\Delta v_{\text{Ly}\alpha}$  in B14-65666, we explore correlations between  $\Delta v_{\text{Ly}\alpha}$ ,  $\text{EW}_0(\text{Ly}\alpha)$ , and  $M_{\text{UV}}$  at  $z \approx 6 - 8$  based on 17 galaxies in Table 9. In addition, given a possible connection between Ly $\alpha$  and [CII] (e.g., Harikane et al. 2017; Carniani et al. 2017b), we also investigate the relation between  $\Delta v_{\text{Ly}\alpha}$  and [CII] luminosities for the first time. Figure 9 shows  $\Delta v_{\text{Ly}\alpha}$  values plotted against  $\text{EW}_0(\text{Ly}\alpha)$ ,  $M_{\text{UV}}$ , and [CII] luminosities. To evaluate the significance of the relation, we perform Spearman rank correlation tests.

In the left panel of Figure 9, the correlation is weak in contrast to the results at  $z \approx 2 - 3$ . It is possible that the correlation at  $z \approx 6 - 8$  is diluted because both  $\Delta v_{\text{Ly}\alpha}$  and  $\text{EW}_0(\text{Ly}\alpha)$  values are affected by the IGM attenuation effect. A large number of objects with  $\Delta v_{\text{Ly}\alpha}$  measurements are needed to conclude if the correlation exists or not at  $z \gtrsim 6$ . Nevertheless, we note that the scatter of  $\Delta v_{\text{Ly}\alpha}$  value becomes larger for smaller  $\text{EW}_0(\text{Ly}\alpha)$  galaxies. Such a trend is consistent with results at  $z \approx 2 - 3$  as shown in the left panel of Figure 10, where we have added the data points of Erb et al. (2014) and the average relation determined in Nakajima et al. (2018). Theoretically, the

trend is explained as a secondary effect of Ly $\alpha$  radiative transfer caused by the viewing angle of galaxy disks (Zheng & Wallace 2014).

In the middle panel of Figure 9, we confirm a  $4.5\sigma$  correlation between  $M_{UV}$  and  $\Delta v_{Ly\alpha}$ , indicating that brighter  $M_{UV}$  objects have larger  $\Delta v_{Ly\alpha}$ . Although the trend is consistent with that at  $z \approx 2 - 3$ , we have identified the trend at  $z \approx 6 - 8$  for the first time.

In the right panel of Figure 9, we identify a positive correlation at the significance level of  $4.0\sigma$ , indicating that galaxies with higher [CII] luminosities have larger  $\Delta v_{Ly\alpha}$  values. The correlation can be also explained in a context of the neutral gas content. Based on observations of our Galaxy and some nearby galaxies, previous studies have shown that the [CII] luminosity becomes higher for larger  $N_{HI}$  regions (e.g., Bock et al. 1993; Matsuhara et al. 1997). Physically, this is due to the fact that [CII] is dominantly emitted from the neutral gas.

In summary, the middle and right panels of Figure 9 imply that  $\Delta v_{Ly\alpha}$  values at  $z \approx 6 - 8$  are regulated by the neutral gas content in the ISM, which is similar to the result at  $z \approx 2 - 3$ . This indicates that the large  $\Delta v_{Ly\alpha}$  in B14-65666 would be due to its large  $N_{HI}$  value.

## 8 Discussion

### 8.1 A consistent picture of B14-65666

B14-65666 is the first object with a complete set of [CII], [OIII], and dust continuum emission in the reionization epoch. In conjunction with the HST F140W data (Bowler et al. 2017) and the Ly $\alpha$  line (Furusawa et al. 2016), the rich data allow us to discuss the properties of B14-65666 in detail.

As shown in the top left panel of Figure 4, B14-65666 shows two rest-frame UV clumps whose spatial positions are consistent with those of two [CII] knots. Our high angular resolution data also reveal that [CII] and [OIII] show velocity gradients of  $\approx 200 \text{ km s}^{-1}$  (the bottom panels of Figure 4). High- $z$  velocity gradients are often interpreted in the context of merger (e.g., Jones et al. 2017a; Carniani et al. 2017b) or rotational disks (e.g., Jones et al. 2017b; Smit et al. 2018). For example, Jones et al. (2017a) have concluded that a galaxy at  $z = 6.07$ , WMH5, would be merger rather than a rotational disk based on two separated [CII] clumps, the [CII] velocity gradient, and the [CII] spectral line composed of multiple Gaussian profiles. The same is also the case for B14-65666. Based on the UV and [CII] morphology, velocity gradients, and the fact that the high- $S/N$  [CII] line is composed of two Gaussian profiles (Figure 3), we infer that the velocity gradient is due to merger rather than a rotational disk.

The merger scenario is also supported from our SED-fitting results (§6.2). We have shown that single stellar component models result in a young stellar age ( $\approx 5 \text{ Myr}$ ) which cannot

reproduce the large dust mass of B14-65666,  $\approx (1 - 6) \times 10^7 M_{\odot}$ . Instead, we have demonstrated that two component models with past star-forming activity is necessary to reproduce the dust mass. These results imply that the current star formation activity is induced by the merger event. A merger event would enhance the star forming activity. Based on the two component models, we calculate the current high specific SFR, defined as the SFR per unit stellar mass ( $sSFR \equiv SFR/M_*$ ). The  $sSFR$  of  $68 \pm 47 \text{ Gyr}^{-1}$  is comparable to or larger than those for galaxies on the star formation main sequence at  $z \approx 6 - 7$  (e.g., Stark et al. 2013; Speagle et al. 2014; Santini et al. 2017). This suggests that B14-65666 is undergoing bursty star-formation (Rodighiero et al. 2011).

In conclusion, based on the morphologies of UV and [CII], velocity gradients of [CII] and [OIII], the large dust mass and the SED-fitting results, we infer that B14-65666 is a merger-induced starburst.

### 8.2 Ly $\alpha$ velocity offsets at $z \approx 6 - 8$ and implications for reionization

In this section, we discuss implications on reionization from the compiled  $\Delta v_{Ly\alpha}$  measurements at  $z \approx 6 - 8$ .

#### 8.2.1 Enhanced Ly $\alpha$ visibility for bright galaxies

The Ly $\alpha$  velocity offset at  $z \approx 6 - 8$  is useful to constrain the reionization process as described below. Based on spectroscopic observations of LAEs and LBGs, previous studies have shown that the fraction of galaxies with strong Ly $\alpha$  emission increases from  $z = 2$  to 6 (e.g., Cassata et al. 2015), but suddenly drops at  $z > 6$  (e.g., Stark et al. 2010; Pentericci et al. 2011; Ono et al. 2012; Schenker et al. 2012, 2014). This is often interpreted as a rapid increase of the neutral gas in the IGM at  $z \approx 6$ , significantly reducing the visibility of Ly $\alpha$ . Ono et al. (2012) have revealed that the amplitude of the drop is smaller for UV bright galaxies than for UV faint galaxies. More recently, Stark et al. (2017) have demonstrated a striking LAE fraction of 100% in the sample of most luminous LBGs (Oesch et al. 2015; Zitrin et al. 2015; Roberts-Borsani et al. 2016). Stark et al. (2017) have discussed possible origins of the enhanced Ly $\alpha$  visibility of these UV luminous galaxies, one of which is that their large Ly $\alpha$  velocity offsets make Ly $\alpha$  photons less affected by the IGM attenuation when Ly $\alpha$  photons enter the IGM.

In the middle and right panels of Figure 9, we have statistically demonstrated that the  $\Delta v_{Ly\alpha}$  value becomes larger for galaxies with brighter UV or [CII] luminosities at  $z \approx 6 - 8$ . This means that the Ly $\alpha$  visibility is indeed enhanced in brighter galaxies (see also Mainali et al. 2017; Mason et al. 2018), which would give us a reasonable explanation on the high Ly $\alpha$  fraction in luminous galaxies.

**Table 9.**  $\Delta v_{\text{Ly}\alpha}$  literature sample

Name	Lines	$z_{\text{sys}}$	$\Delta v_{\text{Ly}\alpha}$ (km s <sup>-1</sup> )	$M_{\text{UV}}$ (AB mag.)	$\text{EW}_0(\text{Ly}\alpha)$ (Å)	$L([\text{CII}])$ (10 <sup>7</sup> L <sub>⊙</sub> )	$\mu$	Ref.
(1)	(2)	(3)	(4)	(5)	(6)	(7)	(8)	(9)
A2744_YD4	[OIII]	8.38	70	$-20.9 + 2.5 \log(\mu)$	$10.7 \pm 2.7$	NA <sup>a</sup>	$1.8 \pm 0.3$	L17
EGS-zs8-1	CIII]1907, 1909	7.72	$340^{+15}_{-30}$	-22.1	$21 \pm 4$	NA <sup>a</sup>	-	St17
SXDF-NB1006-2	[OIII]	7.21	$110 \pm 30$	-21.5	33.0	$8.3 < (3\sigma)$	-	Sh12, I16
B14-65666	[CII], [OIII]	7.15	$772 \pm 45$	-22.3	$3.7^{+1.7}_{-1.1}$	$133 \pm 13$	-	B14, F16, This Study
COSMOS13679	[CII]	7.14	135	-21.5	15	7.12	-	P16
BDF-3299 (clump I)	[CII]	7.11	71	-20.9	50	$4.9 \pm 0.6$	-	V11, Maio15, Ca17a
A1703-zd6	OIII]1666	7.04	60	$-21.1 + 2.5 \log(\mu)$	$65 \pm 12$	NA <sup>a</sup>	5.2	Sc12, St15b
RXJ1347.1-1145	[CII]	6.77	$20^{+140}_{-40}$	$-20.8 + 2.5 \log(\mu)^b$	$26 \pm 4$	$7.0^{+1.0}_{-1.5}/\mu^b$	$5.0 \pm 0.3$	B17
NTTDF6345	[CII]	6.70	110	-21.6	15	17.7	-	P16
UDS16291	[CII]	6.64	110	-21.0	6	7.15	-	P16
COSMOS24108	[CII]	6.62	240	-21.7	27	10.0	-	P16
CR7 (full)	[CII]	6.60	$167 \pm 22$	-22.2	$211 \pm 20$	$21.7 \pm 3.6^c$	-	S15, Mat17
Himiko (Total)	[CII]	6.59	$145 \pm 15$	-21.9	$78^{+8}_{-6}$	$12 \pm 2$	-	O13, Ca18
CLM1	[CII]	6.16	$430 \pm 69$	-22.8	50	$24 \pm 3.2$	-	Cu03, W15
RXJ2248-ID3	OIII]1666, CIV	6.11	235	$-22.0 + 2.5 \log(\mu)^d$	$39.6 \pm 5.1$	NA <sup>a</sup>	5.5	Main17
WMH5	[CII]	6.07	$504 \pm 52$	-22.7	13	$66 \pm 7.2$	-	W13, W15
A383-5.1	[CII]	6.03	$68 \pm 85$	$-21.6 + 2.5 \log(\mu)^e$	138	$9.5/\mu$	11.4	R11, K16

Note. Properties of the compiled sample with  $\Delta v_{\text{Ly}\alpha}$  measurements at  $z > 6$  from the literature and this study. Error values are presented if available.

(1) The object name; (2) the emission line(s) used to measure the systemic redshift,  $z_{\text{sys}}$ ; (3) the systemic redshift; (4) the Ly $\alpha$  velocity offset with respect to the systemic redshift; (5) the UV absolute magnitude in the AB magnitude system; (6) the rest-frame Ly $\alpha$  equivalent width; (7) the [CII] luminosity; (8) the lensing magnification factor; (9) references.

<sup>a</sup> 'NA' indicates that the [CII] luminosity is not available.

<sup>b</sup> Values before corrected for magnification are inferred from B17 under the assumption of  $\mu = 5.0$ .

<sup>c</sup> Aperture luminosity in M17 is adopted (see Table 1 of Mat17).

<sup>d</sup> Values before corrected for magnification are inferred from Main17 under the assumption of  $\mu = 5.5$ .

<sup>e</sup> Inferred from  $Y = 26.15$

Reference Cu03: Cuby et al. (2003), R11: Richard et al. (2011), V11: Vanzella et al. (2011), O12: Ono et al. (2012), Sc12: Schenker et al. (2012), Sh12: Shibuya et al. (2012), W13: Willott et al. (2013), Maio15: Maiolino et al. (2015), W15: Willott et al. (2015), So15: Sobral et al. (2015), St15a: Stark et al. (2015b), St15b: Stark et al. (2015a), K16: Knudsen et al. (2016), P16: Pentericci et al. (2016), I16: Inoue et al. (2016), St17: Stark et al. (2017) B17: Bradač et al. (2017), Ca17a: Carniani et al. (2017a), Ca18: Carniani et al. (2018), L17: Laporte et al. (2017), Mat17: Matthee et al. (2017), Mail17: Mainali et al. (2017).

### 8.2.2 Redshift evolution of $\Delta v_{\text{Ly}\alpha}$

We now turn our attention to redshift evolution of  $\Delta v_{\text{Ly}\alpha}$ . In Figure 10, we compare  $\Delta v_{\text{Ly}\alpha}$  values at two redshift bins of  $z \approx 2 - 3$  and  $z \approx 6 - 8$ , where low- $z$  bin sample is taken from Erb et al. (2014).

In the middle panel, there is a clear trend that  $\Delta v_{\text{Ly}\alpha}$  values at high- $z$  bin are smaller than those at low- $z$  bin at a given  $M_{\text{UV}}$  value, as claimed by Mason et al. (2017) based on a compiled sample of  $N = 10$  objects at  $z \approx 6 - 8$  (see also Mainali et al. 2017 and Stark et al. 2017). However, as discussed in detail by Mason et al. (2017), it may not be appropriate to compare  $\Delta v_{\text{Ly}\alpha}$  values at a given  $M_{\text{UV}}$  value to investigate redshift evolution of  $\Delta v_{\text{Ly}\alpha}$ : Properties of galaxies with the same  $M_{\text{UV}}$  values may be different at different redshifts.

Therefore, following Mason et al. (2017), we investigate the  $\Delta v_{\text{Ly}\alpha}$  values at a given halo mass,  $M_h$ , to examine redshift evolution of  $\Delta v_{\text{Ly}\alpha}$ . To do so, we use the relation between  $M_{\text{UV}}$  and  $M_h$  obtained by Harikane et al. (2018) based on clustering analyses (see their Fig. 15; see also Harikane et al. 2016). Because the 17 galaxies at  $z \approx 6 - 8$  have a mean redshift of 6.8, we use the  $M_{\text{UV}}-M_h$  relation of Harikane et al. (2018) at

$z = 7$ . The right panel of Figure 10 shows the derived  $M_h-\Delta v_{\text{Ly}\alpha}$  relation. For a reference, we also show in blue circles the  $M_h-\Delta v_{\text{Ly}\alpha}$  relation assuming the  $M_{\text{UV}}-M_h$  relation at  $z = 6$  of Harikane et al. (2018).

To discuss redshift evolution of  $\Delta v_{\text{Ly}\alpha}$ , we confine the sample into objects with  $11.2 < \log_{10}(M_h/M_\odot) < 13.0$ . As can be seen from the right panel of Figure 10, the two redshift samples are equally populated in the halo mass range. Figure 11 shows histograms of  $\Delta v_{\text{Ly}\alpha}$  values of the subsamples. We obtain the median  $\Delta v_{\text{Ly}\alpha}$  value of  $156 \pm 52$  km s<sup>-1</sup> and  $327 \pm 16$  km s<sup>-1</sup> at  $z \approx 6 - 8$  and at  $z \approx 2 - 3$ , respectively, where error values represent standard error values. To statistically evaluate the similarity or difference of the  $\Delta v_{\text{Ly}\alpha}$  distributions at the two redshift bins, we also perform the two-sample Kolmogorov-Smirnov (K-S) test. We obtain the  $p$  value of 0.019, indicating that the two distributions may be statistically different, although a larger sample with  $\Delta v_{\text{Ly}\alpha}$  measurements is useful to obtain a definitive conclusion. Thus, we find a tentative trend that the  $\Delta v_{\text{Ly}\alpha}$  value becomes smaller at higher- $z$ .

The  $\Delta v_{\text{Ly}\alpha}$  value at  $z \approx 6 - 8$  is crucial to estimate the neutral gas fraction in the IGM,  $\chi_{\text{HI}}$ , based on results of the de-

# Ly $\alpha$ velocity offset at $z \approx 6-8$

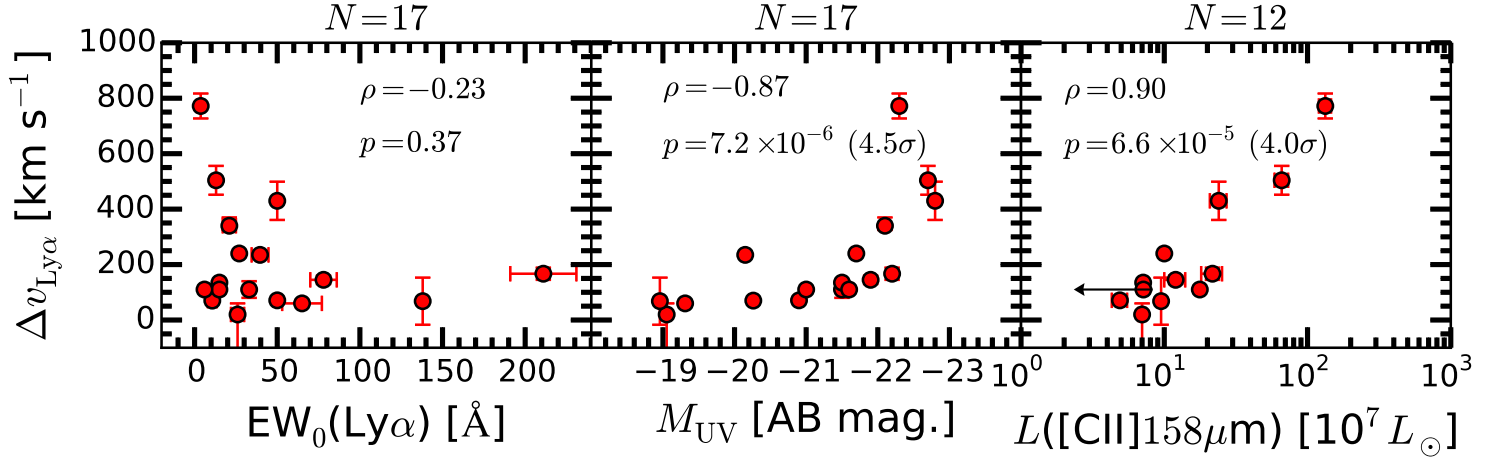


**Fig. 9.** Compilation of Ly $\alpha$  velocity offsets at  $z \approx 6-8$  from this study and the literature (Table 9). The  $\Delta v_{\text{Ly}\alpha}$  value is plotted against  $\text{EW}_0(\text{Ly}\alpha)$  (left panel),  $M_{\text{UV}}$  (middle panel), and the [CII] 158  $\mu\text{m}$  luminosity (right panel). Error bars for the literature sample are shown if available. In each panel,  $N$  shows the number of individual data points. In the middle and right panels, the values of  $M_{\text{UV}}$  and [CII] luminosity are corrected for magnification factors. In each panel,  $\rho$  indicates the Spearman rank correlation coefficient for the relation, and  $p$  denotes the probability satisfying the null hypothesis.

## Comparisons of $\Delta v_{\text{Ly}\alpha}$

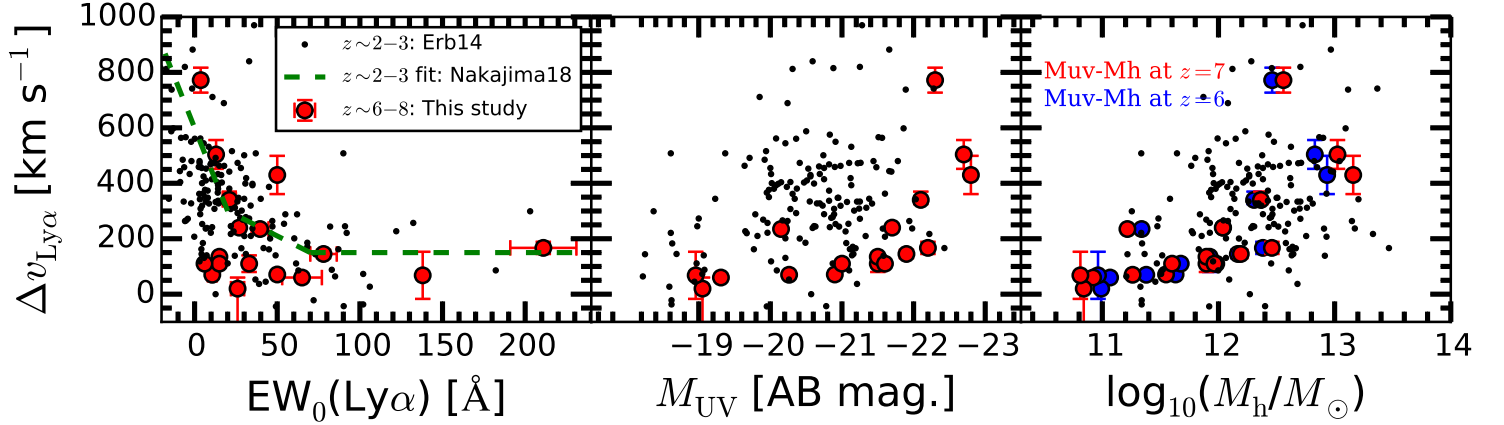


**Fig. 10.** Comparisons of  $\Delta v_{\text{Ly}\alpha}$  at  $z \approx 6-8$  and at  $z \approx 2-3$  as a function of  $\text{EW}_0(\text{Ly}\alpha)$ ,  $M_{\text{UV}}$ , and the halo mass  $M_{\text{h}}$ . To obtain  $M_{\text{h}}$ , we have used the  $M_{\text{UV}}-M_{\text{h}}$  relation at  $z = 7$  obtained in Harikane et al. (2018) (see also Harikane et al. 2016). In each panel, the red circles show the data points at  $z \approx 6-8$  whereas black small dots show data points at  $z \approx 2-3$  taken from Erb et al. (2014). In the left panel, the green dashed line indicates the average relation at  $z \approx 2-3$  presented in Nakajima et al. (2018). In the right panel, blue circles show  $M_{\text{h}}$  obtained from the  $M_{\text{UV}}-M_{\text{h}}$  relation at  $z = 6$  as a reference. In the middle and right panels, the values of  $M_{\text{UV}}$  and  $M_{\text{h}}$  are corrected for magnification factors.

crease of the Ly $\alpha$  luminosity function (e.g., Konno et al. 2014; Choudhury et al. 2015). Our small median  $\Delta v_{\text{Ly}\alpha}$  value at  $z \approx 6-8$ ,  $156 \pm 52$  km s $^{-1}$ , indicates that the Ly $\alpha$  transmissivity is significantly reduced at  $z \approx 6-8$ . The redshift evolution of  $\Delta v_{\text{Ly}\alpha}$  would partly explain the sudden drop of the Ly $\alpha$  luminosity function and the LAE fraction (e.g., Ono et al. 2012; Mason et al. 2017). Future Ly $\alpha$  emission models for reionization would need to take the redshift evolution of  $\Delta v_{\text{Ly}\alpha}$  into account for an accurate estimate of  $\chi_{\text{HI}}$ .

## 9 Conclusion

We have conducted high spatial resolution ALMA observations of an LBG at  $z = 7.15$ . Our target, B14-65666, has a bright UV absolute magnitude,  $M_{\text{UV}} \approx -22.3$ , and has been spectroscopically identified in Ly $\alpha$  with a small rest-frame equivalent width of  $\approx 4$  Å. Based on our ALMA Band 6 and Band 8 observations, we have detected spatially resolved [CII] 158  $\mu\text{m}$ , [OIII] 88  $\mu\text{m}$ , and dust continuum emission at  $10.8\sigma$ ,  $5.8\sigma$ , and  $5.3\sigma$ , respectively. B14-65666 is the first object with a complete set

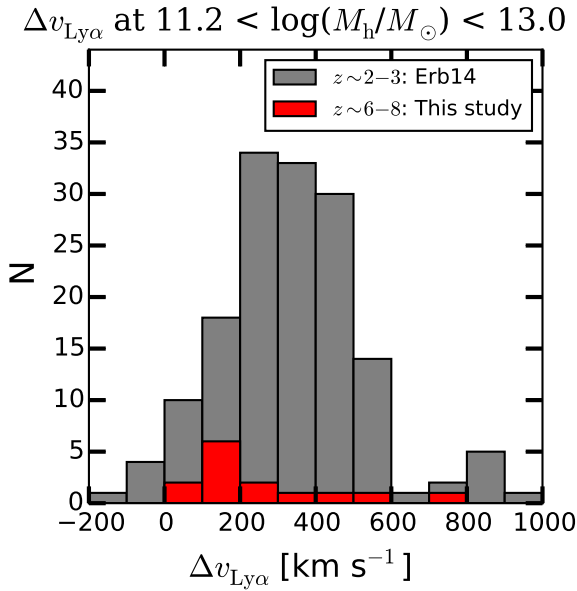


**Fig. 11.** Comparisons of  $\Delta v_{\text{Ly}\alpha}$  at  $z \approx 6-8$  and at  $z \approx 2-3$  at a given halo mass,  $M_h$ . For the compiled sample at  $z \approx 6-8$ , we use the  $M_{\text{UV}}-M_h$  relation at  $z=7$  obtained by Harikane et al. 2018. Two sample K-S tests result in a  $p$  value of 0.019, indicating that the distributions of  $\Delta v_{\text{Ly}\alpha}$  values in the two redshift ranges are statistically different from one another. The  $p$  value is also 0.019 if we use the  $M_{\text{UV}}-M_h$  relation at  $z=6$ . The median  $\Delta v_{\text{Ly}\alpha}$  value is  $156 \pm 52 \text{ km s}^{-1}$  and  $327 \pm 16 \text{ km s}^{-1}$  at  $z \approx 6-8$  and at  $z \approx 2-3$ , respectively.

of Ly $\alpha$ , [OIII], [CII], and dust continuum emission which offers us a unique opportunity to investigate detailed kinematical and ISM properties of high- $z$  galaxies. Our main results are as follows:

- The spatial positions and morphologies of [CII], [OIII], and dust emission are consistent with those of rest-frame UV emission probed by the *HST* F140W image within astrometric uncertainties of  $0''.15$  (Figure 2).
- We have obtained the total [OIII] luminosity,  $(28.6 \pm 4.8) \times 10^8 L_\odot$ , and the total [CII] luminosity,  $(13.3 \pm 1.3) \times 10^8 L_\odot$ . These two luminosities are the highest so far detected among  $z > 6$  star-forming galaxies. The [OIII]-to-[CII] luminosity ratio is  $2.2 \pm 0.4$ . We have created a combined sample of five galaxies with [OIII]-to-[CII] luminosity ratios: Our LBG, two literature LAEs, and a literature SMG comprising of two embedded galaxies. We have found that the luminosity ratio becomes larger for objects with lower bolometric luminosities defined as the sum of the UV and IR luminosities. The results indicate that galaxies with lower bolometric luminosities have either lower metallicities or higher ionization states (§5.2; Figure 6).
- B14-65666 is the highest- $z$  object with a detection of velocity gradients to date. Owing to our high spatial resolution observations, both [CII] and [OIII] reveal velocity gradients of  $\approx 200 \text{ km s}^{-1}$  with projected separations of  $\approx 2-4 \text{ kpc}$ . This is consistent with the fact that the total [CII] 1D spectrum is

comprised of two Gaussian profiles (Figure 3). The spatial positions of velocity peaks are consistent with (i) those of UV emission peaks and (ii) those of two [CII] knots (Figure 4). Based on these results, we infer that B14-65666 is a merger.

- The dust continuum flux density at  $163 \mu\text{m}$  is  $130 \pm 25 \mu\text{Jy}$ , and the  $3\sigma$  upper limit of the dust continuum flux density at  $90 \mu\text{m}$  is  $370 \mu\text{Jy}$ . We have estimated  $L_{\text{TIR}}$  by integrating the modified black-body radiation over  $8-1000 \mu\text{m}$ . Based on the  $3\sigma$  upper limit of the continuum ratio  $S_{\nu,90\mu\text{m}}/S_{\nu,163\mu\text{m}}$  and assuming the emissivity index of  $\beta_d = 1.5$ , we have estimated the dust temperature to be  $< 60 \text{ K}$ . In addition, the CMB temperature at  $z = 7.1520$  indicates that the dust temperature to be  $> 20 \text{ K}$ . With a reasonable assumption of the dust temperature ranging from  $T_d = 30$  to  $50 \text{ K}$ , we obtain  $L_{\text{TIR}} = (1-7) \times 10^{11} L_\odot$ . With a typical dust mass absorption coefficient, the dust mass is estimated to be  $(1-6) \times 10^7 M_\odot$  (§4; Table 5).
- We have investigated the IRX- $\beta$  relation at  $z \approx 6.5-9.1$  based on 10 spectroscopically identified objects including four LBGs with dust continuum detections. For fair comparisons of data points, we have uniformly computed the  $\beta$  and IRX values for the entire sample. We find that the four LBGs with dust detections are well characterized by the Calzetti's dust attenuation curve.
- To estimate the stellar mass, the SFR, and the stellar age, we have performed SED fitting taking ALMA data into account. We have demonstrated how two-component models are necessary to reproduce the estimated dust mass with a reasonable stellar age. Our fiducial two-component model includes an old component which represents underlying past star-formation activity for the duration of  $\approx 200 \text{ Myr}$  in addition to a young secondary starburst component. We have obtained the total stellar mass of  $\approx 2 \times 10^9 M_\odot$ , and the total SFR of  $\approx 140 M_\odot \text{ yr}^{-1}$ . The results support our claims that B14-65666 is an ongoing merger with past star-formation activity (§6; Figure 7).
- The [CII] and [OIII] lines have consistent redshifts of  $z = 7.1520 \pm 0.0003$ . On the other hand, Ly $\alpha$  is significantly redshifted with respect to the ALMA lines by  $\Delta v_{\text{Ly}\alpha} = 772 \pm 45 \text{ km s}^{-1}$ , which is the largest so far detected among the  $z > 6$  galaxy population. The very large  $\Delta v_{\text{Ly}\alpha}$  would be due to the presence of large amount of neutral gas (§7; Figure 8).
- Based on a compiled sample of 17 galaxies at  $z \approx 6-8$  with  $\Delta v_{\text{Ly}\alpha}$  measurements from this study and the literature, we have found a  $4.5\sigma$  ( $4.0\sigma$ ) correlation between  $\Delta v_{\text{Ly}\alpha}$  and UV magnitudes ([CII] luminosities) in the sense that  $\Delta v_{\text{Ly}\alpha}$  becomes larger for brighter UV magnitudes and brighter [CII] luminosities. These results are in a good agreement with a scenario that the Ly $\alpha$  emissivity during the reionization epoch depends on the galaxy's luminosity (§7; Figure 9).
- We have also compared the  $\Delta v_{\text{Ly}\alpha}$  values at  $z \approx 6-8$  with

those at  $z \approx 2 - 3$ . We have statistically shown that, at a given dark matter halo mass, the  $\Delta v_{\text{Ly}\alpha}$  value is smaller at higher- $z$  (§8.2; Figures 10 and 11).

Given the rich data available and spatially extended nature, B14-65666 is one of the best target for follow-up observations with ALMA and *James Webb Space Telescope*'s NIRSpec IFU mode to spatially resolve e.g., gas-phase metallicity, the electron density, and Balmer decrement.

## Acknowledgments

This paper makes use of the following ALMA data: ADS/JAO.ALMA#2016.1.00954.S. ALMA is a partnership of ESO (representing its member states), NSF (USA) and NINS (Japan), together with NRC (Canada), NSC and ASIAA (Taiwan), and KASI (Republic of Korea), in cooperation with the Republic of Chile. The Joint ALMA Observatory is operated by ESO, AUI/NRAO and NAOJ. This work is based in part on data collected at Subaru Telescope, which is operated by the National Astronomical Observatory of Japan. Data analysis were in part carried out on common use data analysis computer system at the Astronomy Data Center, ADC, of the National Astronomical Observatory of Japan. T.H. and A.K.I. appreciate support from NAOJ ALMA Scientific Research Grant Number 2016-01A. We are also grateful to KAKENHI grants 26287034 and 17H01114 (K.M. and A.K.I.), 17H06130 (Y.Tamura), 16H01085 (T.O.), 16H02166 (Y.Taniguchi), 17K14252 (H.U.), JP17H01111 (I.S.), 16J03329 (Y.H.), and 15H02064 (M.O.), JP17H06130 (K.Kohno). E.Z. acknowledges funding from the Swedish National Space Board. K.O. acknowledges the Kavli Institute Fellowship at the Kavli Institute for Cosmology at the University of Cambridge, supported by the Kavli Foundation. K.Knudsen acknowledges support from the Knut and Alice Wallenberg Foundation. We acknowledge Nicolas Laporte, Stefano Carniani, Dan Marrone, and Dawn Erb for providing us with their data. We thank Kouichiro Nakanishi, Fumi Egusa, Kazuya Saigo and Seiji Fujimoto for discussions in handling with ALMA data, and Alcione Mora for help in the GAIA archive data. We are grateful to Rebecca A. A. Bowler, Daisuke Iono, Miju Lee, Kenichi Tadaki, Hidenobu Yajima, Kazuhiro Shimasaku, Shohei Aoyama, Toru Nagao, Masaru Kajisawa, Kyoko Onishi, Takuji Yamashita, Satoshi Yamanaka, Andrea Ferrara, Tanya Urrutia, Sangeeta Malhotra, and Dan Stark for helpful discussions.

## References

- Bañados, E., et al. 2018, *Nature*, 553, 473
- Bock, J. J., et al. 1993, *ApJL*, 410, L115
- Bouwens, R. J., et al. 2009, *ApJ*, 705, 936
- . 2010, *ApJL*, 708, L69
- . 2014, *ApJ*, 795, 126
- . 2016, *ApJ*, 833, 72
- Bowler, R. A. A., Bourne, N., Dunlop, J. S., McLure, R. M., & McLeod, D. J. 2018, *ArXiv e-prints*
- Bowler, R. A. A., Dunlop, J. S., McLure, R. J., & McLeod, D. J. 2017, *MNRAS*, 466, 3612
- Bowler, R. A. A., et al. 2014, *MNRAS*, 440, 2810
- Bradač, M., et al. 2017, *ApJL*, 836, L2
- Brauher, J. R., Dale, D. A., & Helou, G. 2008, *ApJS*, 178, 280
- Bruzual, G., & Charlot, S. 2003, *MNRAS*, 344, 1000
- Calura, F., et al. 2017, *MNRAS*, 465, 54

- Calzetti, D., Armus, L., Bohlin, R. C., Kinney, A. L., Koornneef, J., & Storchi-Bergmann, T. 2000, *ApJ*, 533, 682
- Capak, P. L., et al. 2015, *Nature*, 522, 455
- Carilli, C. L., & Walter, F. 2013, *ARA&A*, 51, 105
- Carniani, S., Maiolino, R., Smit, R., & Amorín, R. 2018, *ApJL*, 854, L7
- Carniani, S., et al. 2017a, *A&A*, 605, A42
- . 2017b, *ArXiv e-prints*
- Casey, C. M. 2012, *MNRAS*, 425, 3094
- Cassata, P., et al. 2015, *A&A*, 573, A24
- Chabrier, G. 2003, *ApJL*, 586, L133
- Chapman, S. C., Blain, A. W., Smail, I., & Ivison, R. J. 2005, *ApJ*, 622, 772
- Chevallard, J., & Charlot, S. 2016, *MNRAS*, 462, 1415
- Choudhury, T. R., Puchwein, E., Haehnelt, M. G., & Bolton, J. S. 2015, *MNRAS*, 452, 261
- Cormier, D., et al. 2015, *A&A*, 578, A53
- Cuby, J.-G., Le Fèvre, O., McCracken, H., Cuillandre, J.-C., Magnier, E., & Meneux, B. 2003, *A&A*, 405, L19
- da Cunha, E., et al. 2013, *ApJ*, 766, 13
- Díaz-Santos, T., et al. 2013, *ApJ*, 774, 68
- Dijkstra, M., Haiman, Z., & Spaans, M. 2006, *ApJ*, 649, 14
- Dunlop, J. S., et al. 2017, *MNRAS*, 466, 861
- Dunne, L., Eales, S., Edmunds, M., Ivison, R., Alexander, P., & Clements, D. L. 2000, *MNRAS*, 315, 115
- Ellis, R. S., et al. 2013, *ApJL*, 763, L7
- Erb, D. K., Steidel, C. C., Shapley, A. E., Pettini, M., Reddy, N. A., & Adelberger, K. L. 2006, *ApJ*, 646, 107
- Erb, D. K., et al. 2014, *ApJ*, 795, 33
- Faisst, A. L., et al. 2017, *ApJ*, 847, 21
- Fudamoto, Y., et al. 2017, *MNRAS*, 472, 483
- Furusawa, H., et al. 2016, *ApJ*, 822, 46
- Gaia Collaboration et al. 2016, *A&A*, 595, A2
- Garel, T., Blaizot, J., Guiderdoni, B., Schaerer, D., Verhamme, A., & Hayes, M. 2012, *MNRAS*, 422, 310
- González-López, J., et al. 2017, *A&A*, 597, A41
- Graciá-Carpio, J., et al. 2011, *ApJL*, 728, L7
- Gronke, M., Bull, P., & Dijkstra, M. 2015, *ApJ*, 812, 123
- Haiman, Z. 2002, *ApJL*, 576, L1
- Harikane, Y., et al. 2016, *ApJ*, 821, 123
- . 2017, *ArXiv e-prints*
- . 2018, *PASJ*, 70, S11
- Hashimoto, T., Ouchi, M., Shimasaku, K., Ono, Y., Nakajima, K., Rauch, M., Lee, J., & Okamura, S. 2013, *ApJ*, 765, 70
- Hashimoto, T., et al. 2015, *ApJ*, 812, 157
- . 2017a, *MNRAS*, 465, 1543
- . 2017b, *A&A*, 608, A10
- . 2018, *ArXiv e-prints*
- Hildebrand, R. H. 1983, *QJRAS*, 24, 267
- Inoue, A. K. 2011a, *MNRAS*, 415, 2920
- . 2011b, *Earth, Planets, and Space*, 63, 1027
- Inoue, A. K., Shimizu, I., Iwata, I., & Tanaka, M. 2014a, *MNRAS*, 442, 1805
- Inoue, A. K., Shimizu, I., Tamura, Y., Matsuo, H., Okamoto, T., & Yoshida, N. 2014b, *ApJL*, 780, L18
- Inoue, A. K., et al. 2016, *Science*, 352, 1559
- Izumi, T., et al. 2018, *ArXiv e-prints*
- Jiang, L., et al. 2013, *ApJ*, 773, 153
- Jones, G. C., Willott, C. J., Carilli, C. L., Ferrara, A., Wang, R., & Wagg, J. 2017a, *ApJ*, 845, 175
- Jones, G. C., et al. 2017b, *ApJ*, 850, 180
- Kashino, D., et al. 2013, *ApJL*, 777, L8
- Katz, H., Kimm, T., Sijacki, D., & Haehnelt, M. G. 2017, *MNRAS*, 468, 4831
- Knudsen, K. K., Richard, J., Kneib, J.-P., Jauzac, M., Clément, B., Drouart, G., Egami, E., & Lindroos, L. 2016, *MNRAS*, 462, L6
- Knudsen, K. K., Watson, D., Frayer, D., Christensen, L., Gallazzi, A., Michałowski, M. J., Richard, J., & Zavala, J. 2017, *MNRAS*, 466, 138
- Komatsu, E., et al. 2011, *ApJS*, 192, 18
- Konno, A., et al. 2014, *ApJ*, 797, 16
- Koprowski, M. P., et al. 2018, *ArXiv e-prints*
- Laporte, N., et al. 2015, *A&A*, 575, A92
- . 2017, *ApJL*, 837, L21
- Laursen, P., Duval, F., & Östlin, G. 2013, *ApJ*, 766, 124
- Madden, S. C., Rémy, A., Galliano, F., Galametz, M., Bendo, G., Cormier, D., Lebouteiller, V., & Hony, S. 2012, in *IAU Symposium*, Vol. 284, *The Spectral Energy Distribution of Galaxies - SED 2011*, ed. R. J. Tuffs & C. C. Popescu, 141–148
- Mainali, R., Kollmeier, J. A., Stark, D. P., Simcoe, R. A., Walth, G., Newman, A. B., & Miller, D. R. 2017, *ApJL*, 836, L14
- Maiolino, R., et al. 2015, *MNRAS*, 452, 54
- Malhotra, S., et al. 1997, *ApJL*, 491, L27
- . 2001, *ApJ*, 561, 766
- Marrone, D. P., et al. 2018, *Nature*, 553, 51
- Mason, C. A., Treu, T., Dijkstra, M., Mesinger, A., Trenti, M., Pentericci, L., de Barros, S., & Vanzella, E. 2017, *ArXiv e-prints*
- Mason, C. A., et al. 2018, *ArXiv e-prints*
- Matsuhara, H., Tanaka, M., Yonekura, Y., Fukui, Y., Kawada, M., & Bock, J. J. 1997, *ApJ*, 490, 744
- Matthee, J., et al. 2017, *ApJ*, 851, 145
- Mawatari, K., Yamada, T., Fazio, G. G., Huang, J.-S., & Ashby, M. L. N. 2016, *PASJ*, 68, 46
- Meurer, G. R., Heckman, T. M., & Calzetti, D. 1999, *ApJ*, 521, 64
- Michałowski, M. J. 2015, *A&A*, 577, A80
- Nakajima, K., Ellis, R. S., Iwata, I., Inoue, A. K., Kusakabe, H., Ouchi, M., & Robertson, B. E. 2016, *ApJL*, 831, L9
- Nakajima, K., Fletcher, T., Ellis, R. S., Robertson, B. E., & Iwata, I. 2018, *ArXiv e-prints*
- Oesch, P. A., Bouwens, R. J., Illingworth, G. D., Labbé, I., & Stefanon, M. 2018, *ApJ*, 855, 105
- Oesch, P. A., et al. 2015, *ApJL*, 804, L30
- Oke, J. B., & Gunn, J. E. 1983, *ApJ*, 266, 713
- Ono, Y., Ouchi, M., Shimasaku, K., Dunlop, J., Farrah, D., McLure, R., & Okamura, S. 2010, *ApJ*, 724, 1524
- Ono, Y., et al. 2012, *ApJ*, 744, 83
- Ota, K., et al. 2014, *ApJ*, 792, 34
- Ouchi, M., et al. 2013, *ApJ*, 778, 102
- Pentericci, L., et al. 2011, *ApJ*, 743, 132
- . 2016, *ApJL*, 829, L11
- Popping, G., Somerville, R. S., & Galametz, M. 2017, *MNRAS*, 471, 3152
- Reddy, N. A., Steidel, C. C., Fadda, D., Yan, L., Pettini, M., Shapley, A. E., Erb, D. K., & Adelberger, K. L. 2006, *ApJ*, 644, 792
- Richard, J., Kneib, J.-P., Ebeling, H., Stark, D. P., Egami, E., & Fiedler, A. K. 2011, *MNRAS*, 414, L31
- Rieke, G. H., Alonso-Herrero, A., Weiner, B. J., Pérez-González, P. G., Blaylock, M., Donley, J. L., & Marcellac, D. 2009, *ApJ*, 692, 556

- Roberts-Borsani, G. W., et al. 2016, *ApJ*, 823, 143
- Rodighiero, G., et al. 2011, *ApJL*, 739, L40
- Santini, P., et al. 2017, *ApJ*, 847, 76
- Sawicki, M. 2012, *PASP*, 124, 1208
- Schaerer, D. 2003, *A&A*, 397, 527
- Schaerer, D., Boone, F., Zamojski, M., Staguhn, J., Dessauges-Zavadsky, M., Finkelstein, S., & Combes, F. 2015, *A&A*, 574, A19
- Schenker, M. A., Ellis, R. S., Konidaris, N. P., & Stark, D. P. 2014, *ApJ*, 795, 20
- Schenker, M. A., Stark, D. P., Ellis, R. S., Robertson, B. E., Dunlop, J. S., McLure, R. J., Kneib, J.-P., & Richard, J. 2012, *ApJ*, 744, 179
- Schinnerer, E., et al. 2007, *ApJS*, 172, 46
- Shibuya, T., Kashikawa, N., Ota, K., Iye, M., Ouchi, M., Furusawa, H., Shimasaku, K., & Hattori, T. 2012, *ApJ*, 752, 114
- Shibuya, T., et al. 2014, *ApJ*, 788, 74
- Smit, R., et al. 2018, *Nature*, 553, 178
- Sobral, D., Matthee, J., Darvish, B., Schaefer, D., Mobasher, B., Röttgering, H. J. A., Santos, S., & Hemmati, S. 2015, *ApJ*, 808, 139
- Speagle, J. S., Steinhardt, C. L., Capak, P. L., & Silverman, J. D. 2014, *ApJS*, 214, 15
- Stark, D. P., Ellis, R. S., Chiu, K., Ouchi, M., & Bunker, A. 2010, *MNRAS*, 408, 1628
- Stark, D. P., Schenker, M. A., Ellis, R., Robertson, B., McLure, R., & Dunlop, J. 2013, *ApJ*, 763, 129
- Stark, D. P., et al. 2015a, *MNRAS*, 454, 1393
- . 2015b, *MNRAS*, 450, 1846
- . 2017, *MNRAS*, 464, 469
- Steidel, C. C., Erb, D. K., Shapley, A. E., Pettini, M., Reddy, N., Bogosavljević, M., Rudie, G. C., & Rakic, O. 2010, *ApJ*, 717, 289
- Takeuchi, T. T., Yuan, F.-T., Ikeyama, A., Murata, K. L., & Inoue, A. K. 2012, *ApJ*, 755, 144
- Trainor, R. F., Steidel, C. C., Strom, A. L., & Rudie, G. C. 2015, *ApJ*, 809, 89
- Valiante, R., Schneider, R., Bianchi, S., & Andersen, A. C. 2009, *MNRAS*, 397, 1661
- Vallini, L., Gallerani, S., Ferrara, A., Pallottini, A., & Yue, B. 2015, *ApJ*, 813, 36
- Vanzella, E., et al. 2011, *ApJL*, 730, L35
- Venemans, B. P., et al. 2012, *ApJL*, 751, L25
- . 2017, *ApJL*, 851, L8
- Verhamme, A., Orlitová, I., Schaefer, D., & Hayes, M. 2015, *A&A*, 578, A7
- Verhamme, A., Schaefer, D., & Maselli, A. 2006, *A&A*, 460, 397
- Verhamme, A., et al. 2018, *ArXiv e-prints*
- Watson, D., Christensen, L., Knudsen, K. K., Richard, J., Gallazzi, A., & Michałowski, M. J. 2015, *Nature*, 519, 327
- Willott, C. J., Carilli, C. L., Wagg, J., & Wang, R. 2015, *ApJ*, 807, 180
- Willott, C. J., Omont, A., & Bergeron, J. 2013, *ApJ*, 770, 13
- Zheng, W., et al. 2014, *ApJ*, 795, 93
- . 2017, *ApJ*, 836, 210
- Zheng, Z., & Wallace, J. 2014, *ApJ*, 794, 116
- Zitrin, A., et al. 2015, *ApJL*, 810, L12